Brodogradnja Volume 75, Number 1 (2024) 75108

journal homepage: www.brodogradnja.fsb.hr

Brodogradnja

An International Journal of Naval Architecture and Ocean Engineering for Research and Development

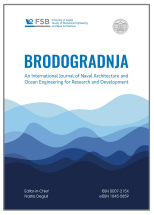

CFD-FEM simulation of water entry of aluminium flat stiffened plate structure considering the effects of hydroelasticity

Jialong Jiao[1]*, *Zhenwei Chen*[1], *Sheng Xu*[2]

[1] *School of Civil Engineering and Transportation, South China University of Technology, Guangzhou 510641, China*
[2] *School of Naval Architecture and Ocean Engineering, Jiangsu University of Science and Technology, Zhenjiang 212000, China*

ARTICLE INFO

Editor-in-Chief: Prof. Nastia Degiuli
Associate Editor: PhD Ivana Martić

Keywords:
Slamming
Water entry
Hydroelasticity
Ship hull structure
Fluid-structure interaction
CFD-FEM

ABSTRACT

In this paper, the slamming loads and structural response of an aluminium flat stiffened-plate structure during calm water entry considering the hydroelasticity effects are studied by a partitioned CFD-FEM two-way coupled method. The target structure is simplified as one segment of an idealized ship grillage structure, comprising flat plate and stiffeners. The typical numerical results are analyzed such as vertical displacement, velocity, acceleration, impact loads, and structural stress of the flexible flat bottom grillage structure considering the hydroelasticity effect and air cushion effect in different free fall height conditions. Drop test results of the same structure and other existing numerical simulation data by both coupled and uncoupled solutions in the literature are used for comparison with the present numerical simulation results. This study provides a practical means to simulate the slamming behaviour and structural response of ship structures, which is useful for predicting ship hull stiffened panel loads and related structural design.

1. Introduction

Water impact phenomena, commonly known as slamming, pose a significant challenge to ships and marine structures due to the strongly nonlinear issue in fluid-structure interaction (FSI) effects. This complex interaction represents a key area of focus within naval architecture and ocean engineering [1,2]. Slamming occurs when a ship bow or stern impacts with water waves at a high relative speed. The resultant slamming loads can cause not only global whipping responses but also local transient vibrations. The prediction of hydrodynamic loads acting on structures and the subsequent structural responses are important for the design of ships and marine structures.

Early researches on slamming loads were usually conducted on the assumption of rigid body structures [3-5], whereas structural flexibility affects slamming behavior in some sense. With the development of large

* Corresponding author.
E-mail address: jiaojl@scut.edu.cn

http://dx.doi.org/10.21278/brod75108
Submitted 28.09.2023; Accepted 28.11.2023.
ISSN 0007-215X; eISSN 1845-5859

and high-speed marine vehicles, the effects of hydroelasticity on local impacts began to attract attention due to high impact velocity and the use of lightweight steel materials. Hydroelasticity is a phenomenon concerned with the mutual interactions among inertial, hydrodynamic and elastic forces. Faltinsen [6] indicated that considering hydroelasticity becomes necessary when the angle between the impacting free surface and the body surface is small. The importance of hydroelasticity also depends on the impact velocity and the natural period of the local structure. The ratio of impulse duration and structural natural periods can be an important factor in the analysis of dynamic structural responses. When the impulse duration is close to or matches the natural period of the structure, it can lead to resonance and result in the significant amplification of structural responses.

The slamming pressures and structural responses on simplified structures such as wedge, sphere, cone, or cylinder have been analyzed extensively [7-9]. Sun et al. [10] investigated the hydrodynamic behaviour of a two-dimensional rigid-body wedge during wave water entry by using an incompressible velocity potential theory. Zhang et al. [11] studied the hydroelasticity in the water entry of flexible wedges considering the flow detachment effect by combining Wagner theory and the modal superposition method. Sun et al. [12] investigated the water entry impact of a cone body with waves by a fully nonlinear boundary element method. Tang et al. [13] predicted the slamming load based on the time-domain Rankine method.

Water impacts on flat plate-shaped structures occur rather frequently in the field of marine engineering. Different from the water entry of structures with a non-zero dead-rise angle, the effect of air cavitation on the impact behaviour of horizontal plate is non-negligible due to the air trapping and air pocket effects. Chuang [14] revealed the effect of air cushion on slamming behaviour. When the air cushion effects are considered, the maximum impact pressure decreases and the impact duration increases. Studies focusing on the slamming loads of a simplified flat-plate structure have been frequent [15-18]. For example, Yan et al. [18] carried out fluid-structure interaction simulations of the water entry of a 4.7 mm thick flat plate made from polyoxymethylene copolymers and compared it with a 12.0 mm thick aluminium bottom plate that was treated as a rigid body. Wang et al. [19] investigated the influence of elasticity on the slamming results by comparing rigid and flexible model simulations. Fang et al. [20] analyzed the slamming load and air-cushion effect of flat plate and LNG tank insulation panel during water entry by the multi-phase Riemann-SPH method.

There has been significant research interest regarding the structural response to slamming loads acting on composite structure flat plate. Sun and Wang [21] investigated the hydrodynamic problem of water impact on the stiffened side of elastic stiffened plates by a Multi-Material Arbitrary Lagrangian-Eulerian (MMALE) solver. Wang et al. [22] studied the hydroelastic response and dynamics of sandwich panels subjected to water impacts by experimental and numerical methods. Thus far, most researchers have focused primarily on simplified flat-plate structures while neglecting the more complex ship hull configurations comprising multiple components such as panels, longitudinal stiffeners and transverse frames [23]. Cheon et al. [24] studied the water entry of a simplified deformable stiffened plate (T-profile stiffener mounted on a flat plate) using LS-DYNA software. Truong et al. [25] evaluated the slamming response of flat-stiffened plates by various numerical methods including the FSI method and obtained drop test results for light-ship-like bottom structures. Truong et al. [26],[27] developed a series of methods including empirical formulation and numerical simulation to predict slamming pressure on flexible flat stiffened steel and aluminium plates considering fluid-structure interaction. Xie et al. [23],[28] experimentally and numerically studied hydroelasticity and the water-entry problem of a composite ship-hull grillage structure made of aluminium. The same model is used for investigation in the present paper but with a different numerical method, and the results are compared.

Besides experimental and analytical methods, the advancement of computer science and technology as well as commercial computing codes have facilitated the application of various numerical solutions for studying water entry problems. Examples are the boundary element method (BEM), Smooth Particle Hydrodynamics (SPH), Computational Fluid Dynamics (CFD), and Arbitrary Lagrangian-Eulerian (ALE) algorithm. To appropriately simulate the slamming loads and structural responses on a flexible structure, it is necessary to consider more complex phenomena such as trapped air and the hydroelasticity effect [5, 29].

The coupling between CFD making use of the Reynolds Averaged Navier Stokes (RANS) equations and the 3D Finite element Model (FEM) is commonly used to simulate ship load responses while also considering the slamming pressure [30-34]. For instance, a one-way coupling model between STAR-CCM+ and LS-DYNA was developed by Takami et al. [35] to evaluate the slamming and whipping response of a ship in waves. Monroy et al. [36] discussed a one-way and a two-way coupled effect between the CFD solver (OpenFOAM) and 3D FEM for the hydroelastic simulation of a containership model. A one-way coupled STAR-CCM+ and ABAQUS accounting for the nonlinear time variation in added mass was proposed by McVicara et al. [37] to investigate the slamming-induced bending moment on wave-piercing catamarans at high forward speed. Moreover, cavitation during the water entry of flexible structures such as cylinder and torpedo was also studied using this method by Shi et al. [38] and Sun et al. [39]. Truong et al. [25] compared slamming results such as total vertical force, deformation and pressure by different FSI methods. It is essential to consider the structure collapse failure when the stress exceeds yield stress, which is a hydroelasto-plasticity problem, and the structural nonlinearities involve plasticity and buckling [40]. The CFD-FEM method was also used to solve the viscous-flow hydroelasto-plasticity of ships in large waves by Liu et al. [41].

This paper focuses on the slamming phenomenon of a flat stiffened plate while considering the coupled effects between fluids and structures. This method has been adopted to study the water entry of wedge-shaped grillage structure into calm water and Stokes waves by Chen et al. [34],[42], and the results show good agreement with test results. However, in those work the wedge is made of steel thus the hydroelastic effects and structural deformation is not obvious. Thus, the advantage of FSI algorithm cannot be fully reflected in those cases. In this study, a ship flat bottom structure made of aluminium is used to study the slamming behaviour considering hydroelasticity and air cushion effects. The impact loads and structural response, such as speed, acceleration and stress of the flexible grillage structure considering hydroelasticity effects are analyzed. Moreover, the numerical simulation results are also compared with drop test and other numerical results in the literature.

2. Model description and investigation cases

As an engineering structure, a ship is an assemblage of components, with the bottom structure as one of the most integral parts of the hull. This should be properly designed to provide not only the required overall longitudinal strength of the hull but also the transverse and local strength to withstand the weight of cargo and external loads, such as hydrostatic pressure, wave loads, slamming loads, and grounding loads that act on the bottom of the hull.

In this study, a flat stiffened-plate structure, which is simplified from one block of an idealized ship bottom grillage structure, is used as the research object [23]. The model is made of aluminium for lower hardness to achieve obvious flexible effects. The segment has a dimension of 1.5 m length, 0.9 m width and 0.3 m height. Fig. 1 illustrates the main components of the hull bottom structure, which comprises flat plates and stiffeners. Three bottom longitudinal bones (T-profile) and two side stringers are arranged longitudinally and two ribbed frames are mounted transversely inside the box structure. The weight of the model is 327.5 kg, including the ballast weight of 221 kg. Table 1 presents the main parameters associated with the hull bottom structure. The side plates and transverse bulkheads are much thicker than the bottom plate, so as to provide a rigid supporting boundary condition on the bottom plate edges. The density of deck plate is amplified to act as ballast weight.

The maximum slamming loads occur at the bottom plate, so pressure sensors are placed here. In addition, strain gauges are mounted on the top surface of the wing panel of T-shaped longitudinal bone. Fig. 2 illustrates the locations of the external pressure probe points P1–P8 and the structural stress detection points S1–S6 on the bottom structure. The fluid pressure on the outer surface of the bottom plate is monitored. The uni-directional stress on the top surface of the wing panel along the T-profile longitudinal bone inside the model is monitored.

As listed in Table 2, four conditions are considered for investigation with different free fall heights or water entry speeds of the model. The model undergoes free fall motion under gravitational acceleration and subsequently impacts calm water vertically with one degree-of-freedom released.

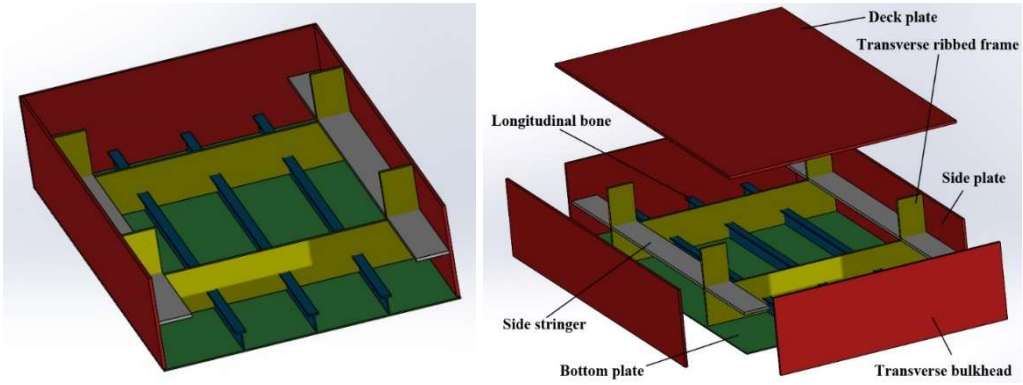

(a) Internal structure (b) Model assembly

Fig. 1 Compositional structure of the hull bottom

Table 1 Main dimension of the wedge structure

Objective	Item	Parameter
Component dimension	Bottom plate thickness (mm)	4
	Side plate thickness (mm)	10
	Deck plate thickness (mm)	10
	Transverse bulkhead thickness (mm)	10
	Bottom longitudinal bone (mm)	$T\frac{5\times30}{5\times50}$
	Side stringer (mm)	100×10
	Transverse ribbed frame plate (mm)	100×10
	Length between transverse frames (mm)	800
	Distance between longitudinal stiffeners (mm)	220
Material property	Mass (kg)	327.5
	Density (kg/m^3)	2700
	Young's modulus (GPa)	72
	Poisson's ratio	0.33

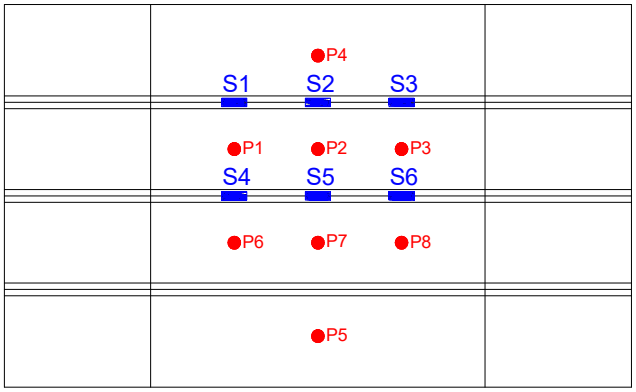

Fig. 2 Monitor points on the structure

Table 2 Experimental conditions in this study

Case ID	1	2	3	4
Free fall height (m)	0.25	0.40	0.55	0.70
Initial speed upon water contact (m/s)	1.68	2.37	2.91	3.36
Initial speed when released (m/s)	1.981	2.620	3.132	3.571

3. Numerical model setup

The CFD-FEM two-way coupling algorithm is applied to study the water entry process of the flat bottom structure. The commercial software STAR-CCM+ and Abaqus are employed as the CFD solver and the FEM solver, respectively. The details of the two-way partitioned coupling algorithm are described below.

3.1 The CFD model

The governing equations for the flow field continuity equation and RANS equation are respectively given as follows:

$$\frac{\partial \overline{u_i}}{\partial x_i} = 0 \tag{1}$$

$$\rho[\frac{\partial \overline{u_i}}{\partial t} + \frac{\partial(\overline{u_i u_j})}{\partial x_j}] = -\frac{\partial \overline{p}}{\partial x_i} + \mu \nabla^2 \overline{u_i} + \frac{\partial}{\partial x_j}(-\rho \overline{u_i' u_j'}) \tag{2}$$

where ρ denotes density, μ denotes turbulent viscosity, t denotes time, u_i denotes velocity component, x_i denotes spatial coordinate component, $\overline{u}$ denotes the time average of velocity, $\overline{p}$ denotes the time average of pressure, $-\rho \overline{u_i' u_j'}$ is the turbulent stress term.

The hydrodynamics of unsteady, viscous, turbulent, and incompressible flow around the hull structure is simulated by Navier–Stokes equations. This study uses the realizable *k-ε* turbulence model, which is more suitable for separation flow and flow with larger streamline curvature. The implicit coupling between fluid pressure and speed is realized by applying the Semi-Implicit Method for Pressure Linked Equations (SIMPLE). The free surface between the water and the air is simulated by applying the Volume of Fluid (VOF) method, which is implemented in STAR-CCM+. The High-Resolution Interface Capturing (HRIC) discretization scheme is utilized to track the interfaces of two-phase flow.

Fig. 3 presents an overview of the model and fluid domain of the numerical wave tank and its boundary conditions. It should be noted that only the external surface geometry is needed for the CFD analysis. The numerical setup consists of a wave tank of 18 m length, 15 m width and 7.5 m depth (including water and air regions). The depth of the water region is 6 m and the air region is 1.5 m. The computational domain is large enough to ignore the tank wall effect. The model with stiffened plate structure is positioned at the center of the tank above the free surface. To satisfy the non-reflection condition, a no-slip wall boundary condition is applied at the five boundary surfaces. On the other hand, the pressure outlet boundary condition is implemented for the top wall.

As can be seen in Fig. 4, the fluid domain consists of a background region and an overset region. The motion responses of the rigid body are simulated by applying the overset mesh technique, while the moving mesh method, i.e., morphing grid technique, is applied to simulate the structural deformation. The overset technique is adopted to simulate large amplitude motions of the structure. In addition, local grid refinement is applied near the model and the free surface to capture detailed flow phenomena accurately. A total of 6.01 million cells are set in the whole computational domain and 2.55 million cells are set in the overset region. To ensure finer resolution near the structure, the thickness of the prism layer increases gradually with a refinement ratio of 1.2. A boundary layer mesh is chosen that consists of 8 cells in the vicinity of the hull structure, with

a target $y+$ value ranging from 30 to 60, which guarantees the accurate representation of the near-wall flow dynamics.

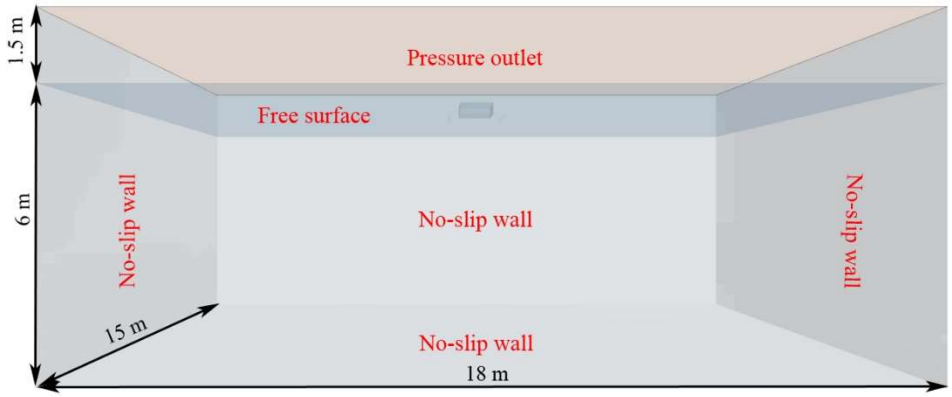

Fig. 3 General view of the numerical wave tank and boundary conditions

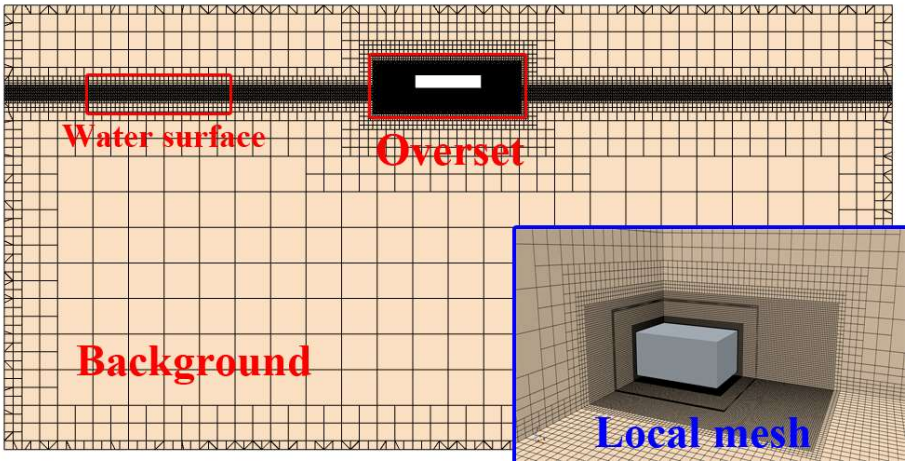

Fig. 4 Mesh generation of the fluid domain

In the numerical setup, the model is assigned with a specific water entry velocity as listed in Table 2. The corresponding initial speed $V_0 = \sqrt{2g(H - H_0)}$ is applied to reduce the calculation cost and the model is positioned at a height of H_0=50 mm over the undisturbed water surface. The FEM solver applies the initial speed listed in Table 2 to the model.

3.2 The FE model

The equation of motion for an elastic isothermal solid can be described by the momentum balance equation:

$$\rho_s \frac{\partial \boldsymbol{u_s}}{\partial t} = \nabla \cdot \boldsymbol{\sigma_s} - \rho_s (\nabla \boldsymbol{u_s}) \boldsymbol{u_s} + \rho_s f_b \tag{3}$$

where $\boldsymbol{u_s} = \dfrac{\partial \boldsymbol{d_s}}{\partial t}$ denotes solid velocity, ρ_s denotes solid density, $\boldsymbol{d_s}$ is the displacement of the elastic structure, $\boldsymbol{\sigma_s}$ represents the Cauchy stress tensor, and f_b is the body force.

The hull segment structure of the FE model was created using the finite element analysis (FEA) software ABAQUS. Fig. 5 shows the established FE model of the hull segment and the generated FE mesh including a local enlarged view. To better visualize the internal structure, the top plate was removed in the figure. The material of the FE model is defined as aluminium. To simulate the ballast weight mounted on the model, the material density of the top plate is adjusted accordingly. The common nodes technique is employed to link the

connected components, which reproduces the welding boundary conditions of the real physical model. The FE model subjects to a variety of loads, including gravitational acceleration loads, prescribed boundary condition loads, and predefined velocity field loads. These applied loads collectively contribute to the comprehensive analysis of the structural behaviour within the FE model. Both the rigid body motions and the structural deformations are solved by the FEA solver based on the pressure and wall shear stress transmitted from the CFD solver by solving the motion control equation.

Deformable three-dimensional shell elements are employed in the FE model for the hull plates and transverse ribbed frame plates. This method is appropriate for accurately capturing the structural behaviour and deformations of the model when the thickness of the plate is much smaller than the length and width. On the other hand, the overall longitudinal bending stiffness of the structure is also reflected by arranging three bottom longitudinal beams (T-profile) using beam elements. Therefore, the model surface is discretized using 4-node quadrilateral reduced shell elements called S4R of 47,700 elements, while the longitudinal beams are discretized using B31 beam elements. The structural model, constructed using a structured grid, comprises a total of 48,150 elements and 47,572 nodes.

This study performs dynamic implicit analysis. To achieve convergence in the simulation process, the initial increment size, minimum increment size and maximum number of increment is set to 10^{-5} s, 10^{-7} s and 10^{7}, respectively. Once several consecutive steps of convergence have been achieved, the increment size will automatically increase to a larger value for subsequent computations.

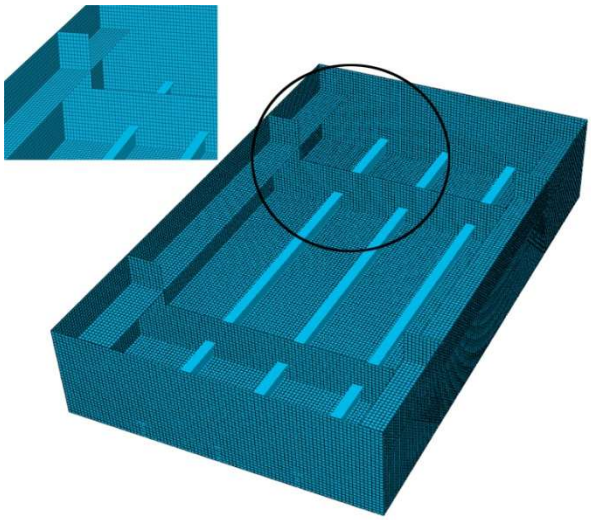

Fig. 5 FE model of the hull bottom structure and mesh generation

Eigenvalue analysis is applied on the FE model to obtain the mode information. Table 3 compares the dry natural frequencies between the numerical and experimental models. It is seen that the 1st order dry natural frequency of the numerical model shows very good agreement with the experimental model, with a difference of 0.8%. The first four orders of modal shape of the numerical model are shown in Fig. 6.

Table 3 Comparison of dry natural frequency between the experimental and the numerical models

Modal order	Experimental (Hz)	Numerical (Hz)	Error (%)
1	35.6	35.9	0.8
2	46.2	50.7	9.7
3	78.2	68.1	–12.9
4	89.6	94.0	4.9

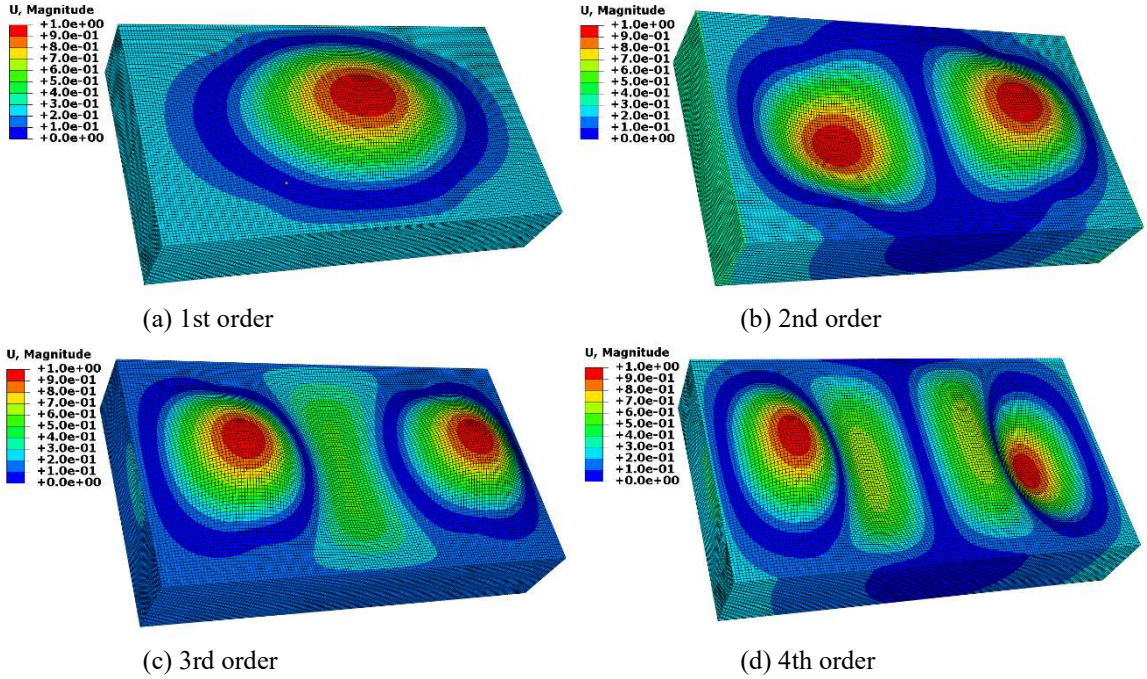

(a) 1st order (b) 2nd order

(c) 3rd order (d) 4th order

Fig. 6 The first four orders of modal shape of the numerical model

3.3 Two-way coupling configuration

One-way coupling is applicable when the deformation of the structure is small and has an ignorable influence on the fluid field. Two-way coupling could also be required even for small deformations in some cases when the hydroelasticity is concerned. The ship loads and hydroelasticity were simulated by both one-way and two-way CFD-FEM coupling schemes and their accuracy and calculation efficiency were compared by Lakshmynarayanana and Hirdaris [43] and Liu et al. [41]. Lakshmynarayanana and Hirdaris [43] concluded that one-way coupling underestimates the high-frequency vibratory components mainly due to the ignorance of added mass effects. Since the hydroelastic effect of the aluminium structure during water entry is pronounced, the two-way coupling method is used in this study to obtain more accurate results.

Fig. 7 illustrates a two-way interaction procedure between the CFD and FEM solvers. For the case of two-way coupling, both the body motions and the structural deformations obtained from the FEA will be fed back to the CFD solver to update the hydrodynamic grid information. The fluid loads on the deformed structure calculated by CFD will then be applied to the structural FE model for the subsequent FEA. The model shell surface serves as the interface for data exchange. Both overset mesh and morpher mesh techniques are implemented in STAR-CCM+. These techniques enable seamless communication and synchronization between the CFD and FEM solvers, which ensures accurate and efficient fluid-structure interaction analysis. In this study, the implicit coupling scheme is employed to accurately capture the FSI problem and hydroelastic effects. The iteration number as well as the number of data exchanges during each coupling time step play a critical role in ensuring the simulation accuracy, so they should be set appropriately. The time step of 0.0001 s is adopted in this present numerical simulation, and the total solution time 0.15 s covers the entire water entry process of the model. The CFD-FEM co-simulations are carried out on workstations equipped with a Threadripper 3990X CPU, featuring 64 cores, a clock speed of 2.9 GHz, and 128 GB of physical memory.

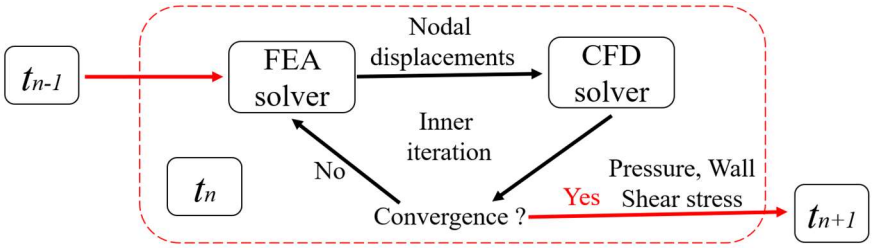

Fig. 7 Two-way coupling procedure during a one-time step interval

4. Verification and validation

4.1 CFD grid size and time step sensitivity

The iteration number, grid size and time step are key contributors to the error and uncertainty in numerical simulations [44-46]. In this study, the sensitivity associated with the uncertainty of CFD grids and time step are evaluated. A comparative view of the three CFD mesh schemes is shown in Fig. 8. Table 4 presents a list of parameters of the three different schemes. It is worth mentioning that the surface grid size of the panel in the fluid domain is half of the basic dimension in the overset region. This is mainly because the FE meshes are usually less precise, while CFD meshes require a finer grid size [34]. The computing time cost is for the simulation of the model's response over approximately 0.15 s of physical time. The maximum Courant number at the steady simulation stage is calculated by the field function provided in the solver. The simulation is considered to be reliable when the Courant number is below 1.0.

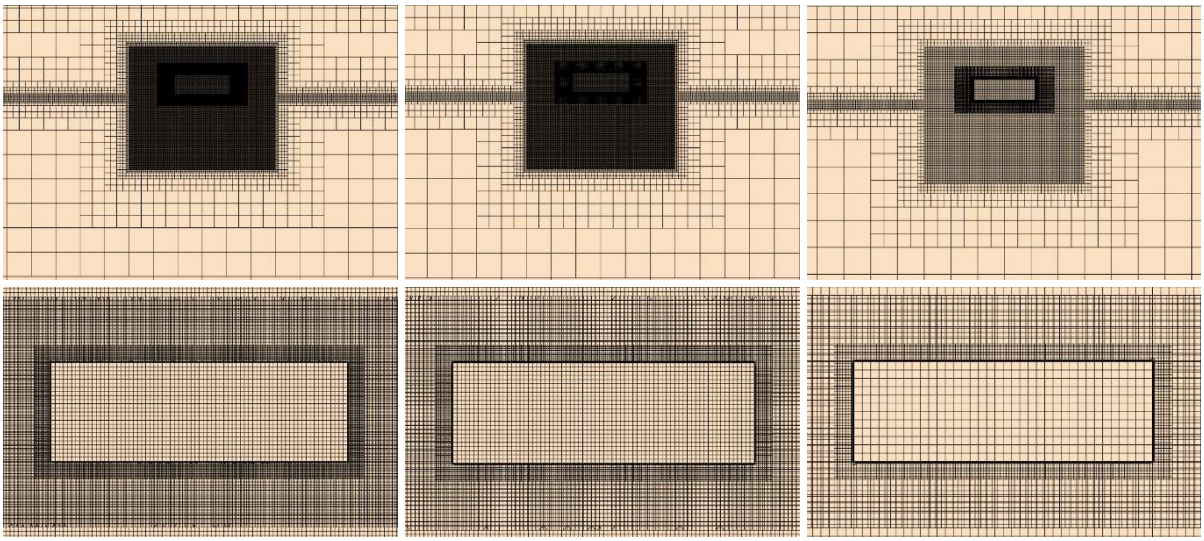

(a) Fine mesh (b) Medium mesh (c) Coarse mesh

Fig. 8 Comparative view of the three CFD mesh schemes

Table 4 Parameters of each scheme

Grid	Δt/s	Cell number (million)			Basic dimension in the overset region (mm)	Basic dimension of plate panel (mm)		Maximum Courant number	Solving time (days)
		Background	Overset	Total		Fluid domain	Structural solver		
Fine	0.00010	8.42	6.57	14.99	8.5	4.25	10	0.449	11.0
Medium	0.00010	6.01	2.55	8.56	12	6	10	0.942	8.5
Coarse	0.00010	2.45	1.00	3.45	17	8.5	10	1.560	6.0
Medium	0.00007	6.01	2.55	8.56	12	6	10	0.804	10.5
Medium	0.00014	6.01	2.55	8.56	12	6	10	1.430	5.0

Fig. 9 and Fig. 10 compare the time series of impact pressure at P1 and stress at S5 by different CFD grids. Table 5 illustrates the verification parameters for the grid size convergence study. As can be observed, all of the signals achieve oscillatory convergence (OC). Moreover, the results show that time step and grid size influence are generally small. Therefore, it is suitable to use the 'Medium' grid in the following analysis.

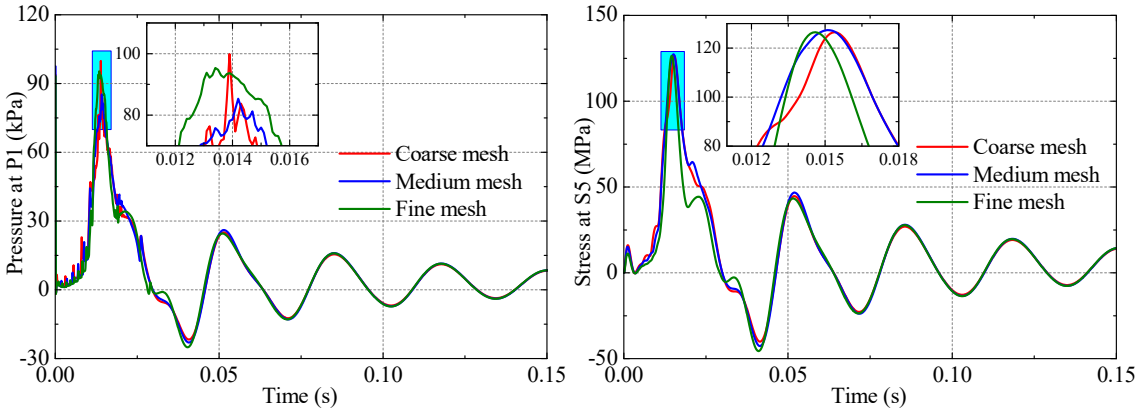

(a) Pressure at P1 (b) Stress at S5

Fig. 9 Comparison of the time series of slamming results for different CFD grid schemes

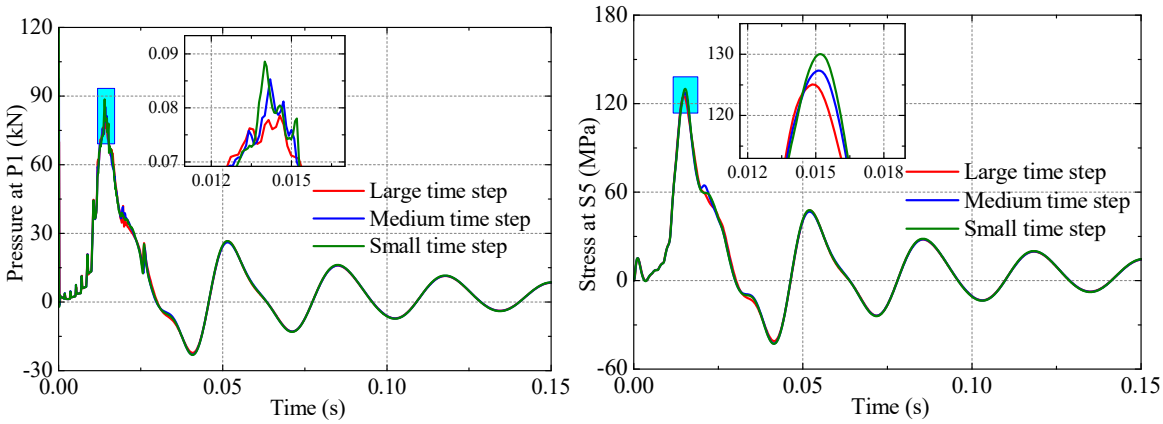

(a) Pressure at P1 (b) Stress at S5

Fig. 10 Comparison of the time series of slamming results for different time step schemes

Table 5 Convergence study for slamming loads for different CFD grid schemes

Parameter		Force crest (kN)	Pressure peak (kPa)		Stress (MPa)
Description	Symbol	F_z	P1	P6	S5
Fine	S_{G1}	109.13	95.34	95.55	126.48
Medium	S_{G2}	99.32	85.28	85.58	127.32
Coarse	S_{G3}	139.61	99.88	99.69	126.45
Change between Medium-fine	$\varepsilon_{G,21}$	9.81	10.06	9.97	–0.84
Change between Coarse-medium	$\varepsilon_{G,32}$	–40.29	–14.60	–14.11	0.87
Convergence ratio	R_G	–0.243	–0.689	–0.707	–0.966
Convergence type	/	OC	OC	OC	OC
Order of accuracy	p_G	N/A	N/A	N/A	N/A
Numerical error	$\delta^*_{REG,1}$	N/A	N/A	N/A	N/A
Uncertainty	U_G	20.145	7.300	7.055	0.435

4.2 Verification of experimental stability

The corresponding free fall tests of the bottom structure model were conducted at the towing tank of Harbin Engineering University (Harbin, China). The experimental setup is illustrated in Fig. 11. During the test, the data of vertical displacement, acceleration, fluid pressure, and structural stress were measured by using four kinds of sensors. A video camera was also used to record the water entry process. More information regarding the experimental setup can be found in the study by Xie et al. [23] [28].

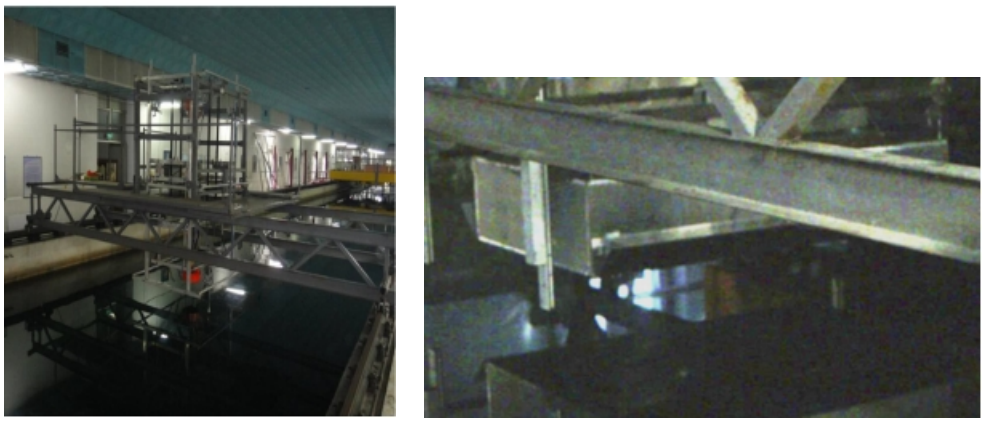

(a) Experimental device (b) Model local view

Fig. 11 Experimental setup of drop test

In order to evaluate the experimental uncertainty and stability, experiments under the same drop condition Case 3 (drop height 0.55 m) were carried out subsequently for three times. Typical signals such as the slamming pressure at P1 and structural stress at S5 measured during the repetitive tests are summarized in Fig. 12. A slight difference can be seen around the peaks of the pressure time series curves. The largest relative error of pressure peak between the three sets of results is within 3.5%. This can be explained by the fact that the slamming pressure is associated with strong nonlinearity and randomicity and can be affected by small disturbances such as air cavitation. The difference in stress signals is below 9.0%, which is larger than the pressure difference. In general, the experimental results are acceptable and stable enough for the purpose of numerical result validation.

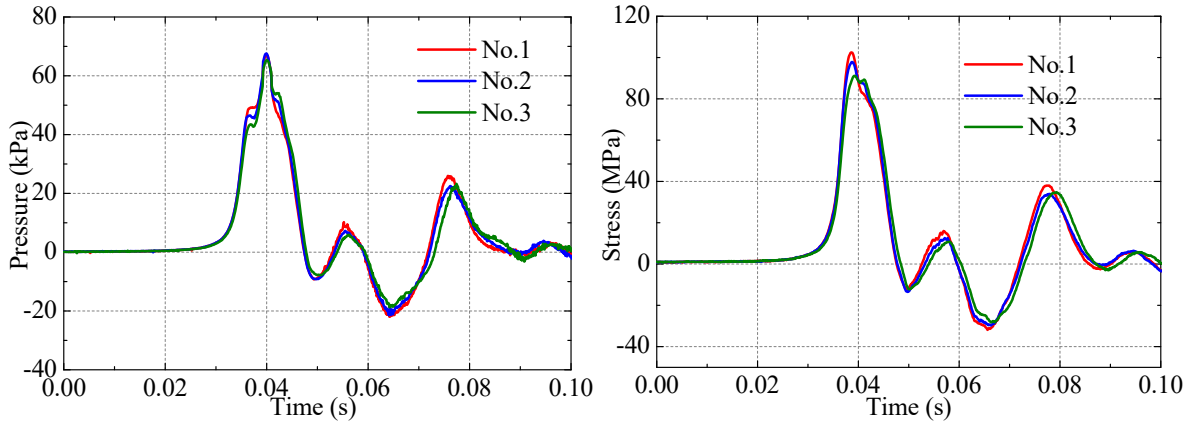

(a) Pressure at P1 (b) Stress at S5

Fig. 12 Comparison of pressure and stress data for experimental repeatability analysis

4.3 Validation of numerical results

Fig. 13 compares the time series of impact pressure at P1 and P2 as well as the structural stress at S2 and S5 for drop heights between Cases 3 and 4 including both the numerical and the experimental results. These generally show good agreement between each other, while the numerical method underestimates the slamming pressure peak and slightly overestimates the structural stress for low-impact velocity cases. Table

6 compares the peak values between the numerical and experimental results. The difference in peak value is generally small with a maximum value of 3.1%. This means that the peak values show good agreement between the numerical and experimental method. However, the difference in the time series results is mainly caused by the high-frequency vibrations, which can be also confirmed from the spectral results obtained using the fast Fourier Transform (FFT) analysis of the time series data in Fig. 14. It is observed that the peak frequency by the numerical method is somewhat greater than the experimental value. The numerical method underestimates the 1st order high-frequency component, while the 2nd order vibration cannot be observed in the experimental results. Only limited time series data are used for spectral analysis as only one slamming event was included. Thus, the adjacent control points in the spectral curve are scattered, which makes the difference seem obvious. The applied numerical computation technique, such as free surface capturing method, mesh generation, time step, and iteration, can also affect the peak value of pressure and stress. Furthermore, the oscillation in the numerical results of the late water entry stage is significantly stronger than that in the experimental ones. This is probably due to the differences in structural damping, local stiffness and mass distribution. The difference in the duration of impact event between the experiment and numerical simulation is mainly caused by the phase difference of high-frequency hydroelastic vibration. Structural damping largely affects the amplitude and phase of high-frequency hydroelastic vibration. Moreover, the distribution and mounting form of ballast weights are not exactly the same for the experimental and the numerical model, which could cause difference in the results especially in the high-frequency hydroelastic response.

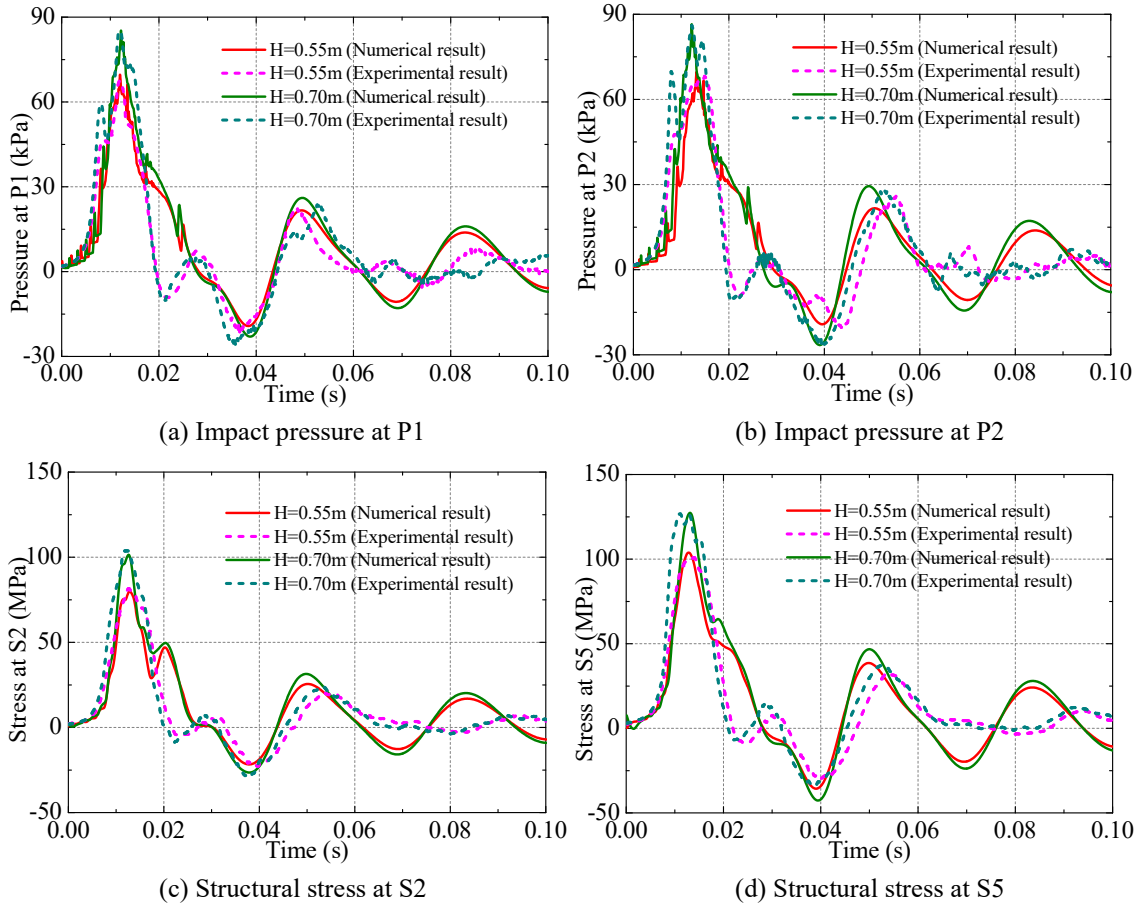

(a) Impact pressure at P1

(b) Impact pressure at P2

(c) Structural stress at S2

(d) Structural stress at S5

Fig. 13 Comparison of time series at different drop heights

Table 6 Comparison of numerical and experimental peak values

Case	Method	P1 (kPa)		P2 (kPa)		S2 (MPa)		S5 (MPa)	
		Peak	Error	Peak	Error	Peak	Error	Peak	Error
H=0.55 m	Numerical	69.65	3.1%	69.67	2.2%	79.71	–2.3%	103.83	2.8%
	Experimental	67.53		68.20		81.61		101.05	
H=0.70 m	Numerical	85.28	0.2%	86.52	0.6%	101.47	–2.5%	127.32	0.3%
	Experimental	85.09		86.04		104.04		126.90	

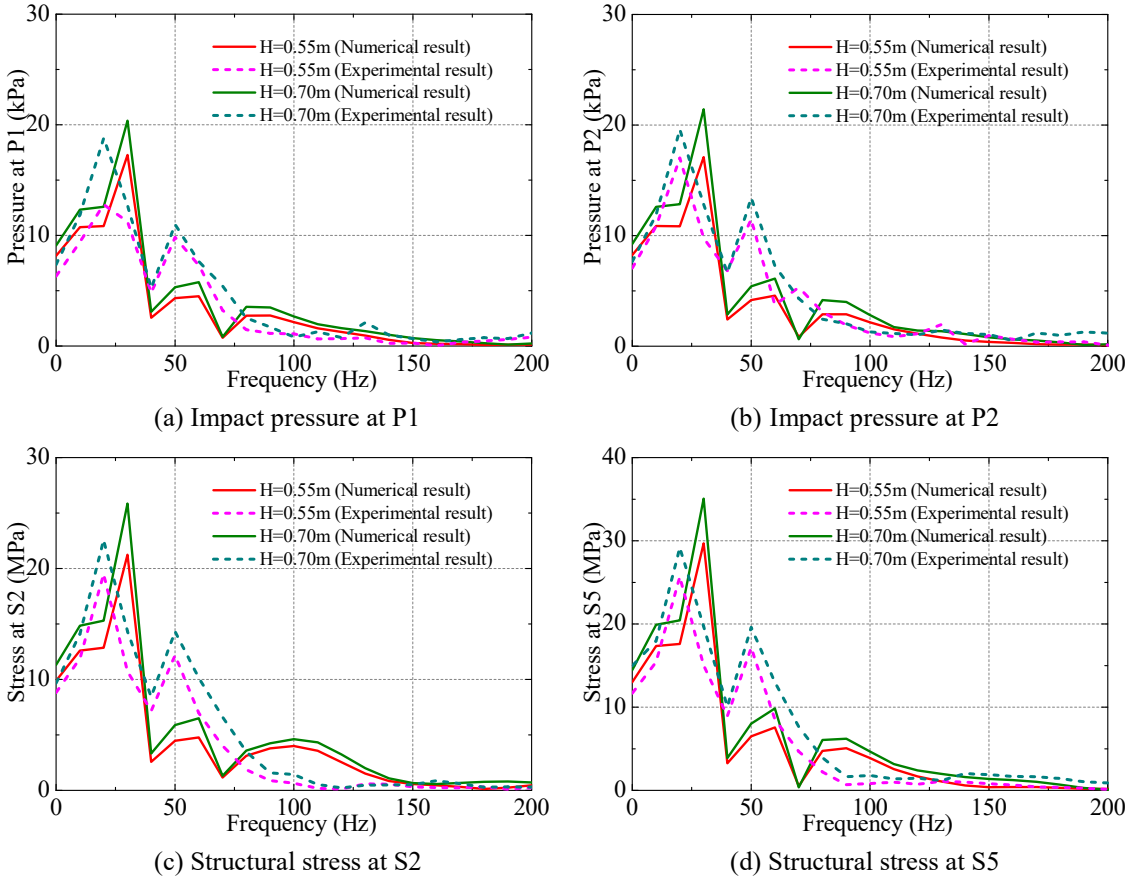

(a) Impact pressure at P1

(b) Impact pressure at P2

(c) Structural stress at S2

(d) Structural stress at S5

Fig. 14 Comparison of spectra at different drop heights

5. Numerical results: analyses and comparisons

5.1 Vertical velocity and acceleration

Fig. 15 presents a comparative analysis of the numerical results for the vertical displacement and velocity for various drop height cases. The initial time zero corresponds to the model located at a position of 50 mm above the calm water surface in all four cases. The displacement curves exhibit two distinct stages of approximate linear variation. The initial stage involves the model free falling in air for a brief duration of approximately 0.01 s before water entry. The second stage of linear variation occurs during the water entry process, with a smaller rate of change. During this phase, the magnitude of the model's speed experiences a significant decline within a short period of time. Subsequently, the speed stabilizes and exhibits small amplitude oscillations due to the elastic deformation of the structure.

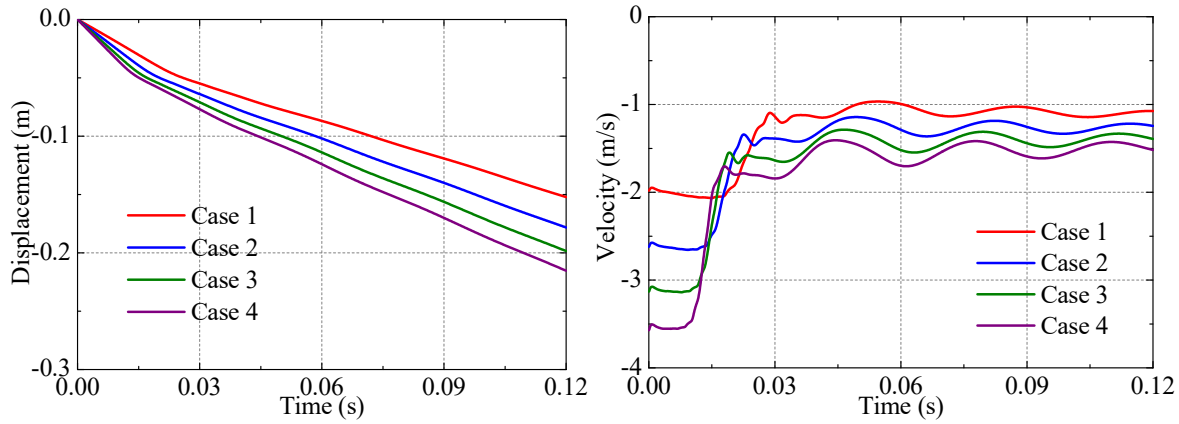

(a) Displacement (b) Velocity

Fig. 15 Vertical motions in different cases by numerical simulation

A comparison of the numerical results of vertical acceleration for different drop heights is presented in Fig. 16, where the time series results at two typical locations, i.e. the center point of the bottom plate and the center point of the side plate, are illustrated. It is found that the acceleration at these two different locations reveals very different behaviour due to structural elastic vibration effects. The high-frequency vibrations are markedly pronounced for the point at the center of the bottom plate due to slamming-induced structural vibrations. However, the high-frequency vibration is not too obvious for the point at the center of the side plate as the structural vertical vibration on the vertical plate is very weak. It is noted that the oscillation can be also observed in Fig. 16(b) due to the structure's overall motion. The peak value and fluctuation amplitude of acceleration increases with the elevation of initial speed from Case 1 to 4 for both points.

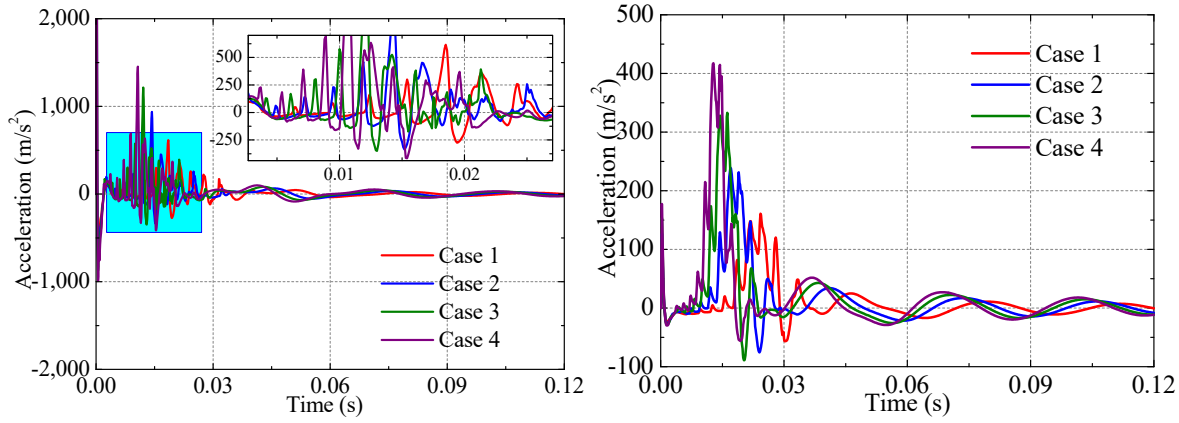

(a) Bottom plate center (b) Side plate center

Fig. 16 Vertical acceleration in different cases by numerical simulation

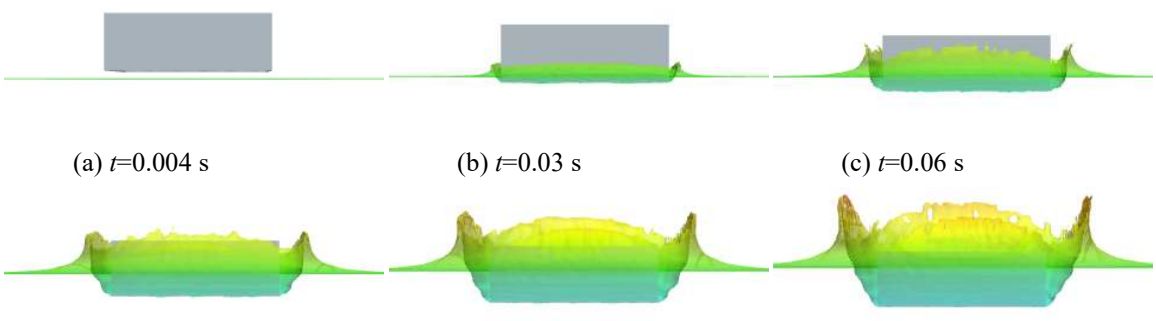

(a) t=0.004 s (b) t=0.03 s (c) t=0.06 s

(d) t=0.09 s (e) t=0.12 s (f) t=0.15 s

Fig. 17 Variation in free surface elevation during water entry (Case 4)

Fig. 17 shows the CFD-simulated fluid flow around the model at typical time instants during the water entry procedure for Case 4. It is found that the CFD solver well simulates and captures some complex flow details around the model such as fluid separation and jet phenomena induced by slamming. Owing to the presence of bilge appendage, the jet flow and water pile-up phenomena are formed. Additionally, Fig. 18 presents a comparison of the free surface and flow field around the model observed from the same view direction between the experimental and numerical simulation. It is evident that there is a satisfactory level of agreement between the two approaches in terms of the depiction of the water pile up and jet flow.

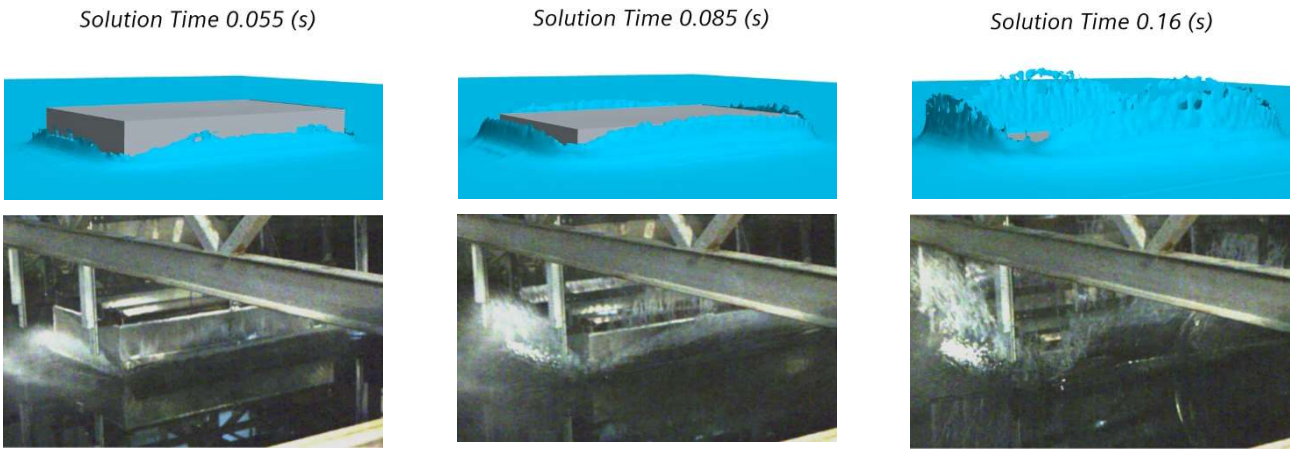

Fig. 18 Comparison of experimental and numerical flow field (Case 4)

5.2 Slamming impact pressure

5.2.1 Pressure distribution and symmetry

This study focuses on the pressure distribution on the bottom surface in typical cases of Case 2 and Case 4. Fig. 19 presents a comparison of the pressure time series at different measuring points. The pressure peaks at P2 and P7 are slightly higher than those at P1 and P6, although the difference is small. This is mainly caused by the longitudinal difference in structural vibration and deformation as well as the air cushion effect. Due to the symmetry of the structure and flow field, the pressure curves at P1 and P6 exhibit a high level of agreement. Furthermore, the results indicate that although slight differences can be observed between P4 and P5, a good symmetry of pressure can be achieved between the two sides. Notably, the pressure peak significantly decreases from the centerline towards the side edge. For instance, the pressure peak at P1 is greater than that at P4. When the compressibility of air cushion is taken into account, the pressure will exhibit a higher peak and shorter slamming impact duration. The air compressibility also obviously affects the aftereffect of pressure oscillation, which manifests in a tendency of sharp crest and flat trough in the curve.

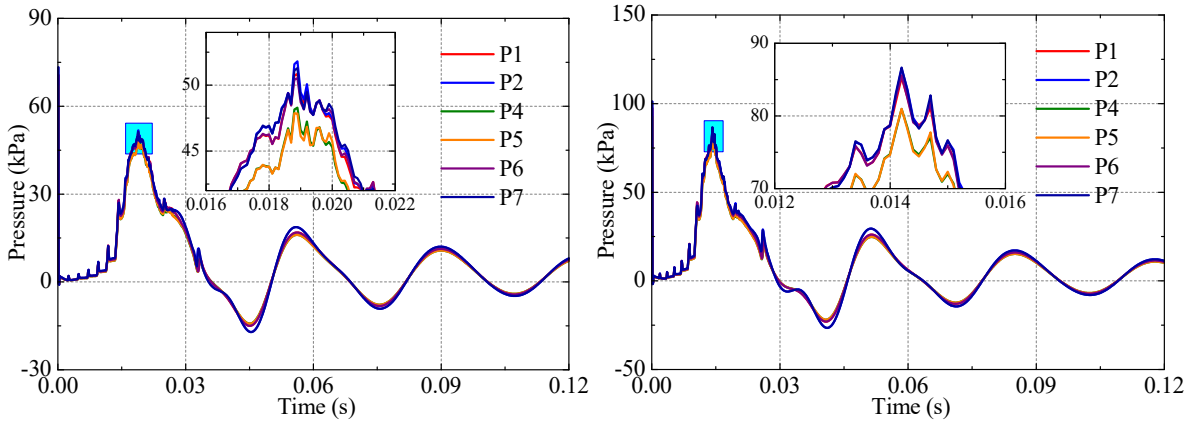

Fig. 19 Time series of pressure at different positions

The evolution of fluid pressure distribution in the flow domain at the middle longitudinal cross-section of the model for Case 4 is illustrated in Fig. 20, where the instantaneous free surface is shown by a black curve. The pressure distributes uniformly at the beginning (t=0.004 s). At t=0.008 s, the pressure around the free surface is disturbed due to the flow speed disturbance effect, although the bottom of the structure does not contact the water. Subsequently, high pressure occurs at the bottom area and the high-pressure area concentrates on the bottom center. As the model moves downward, the pressure distribution on the bottom surface tends to be small. Fig. 21 shows the corresponding pressure distribution on the bottom surface of the model. It can be seen that the pressure decreases from the center to the four edges gradually for all time instants.

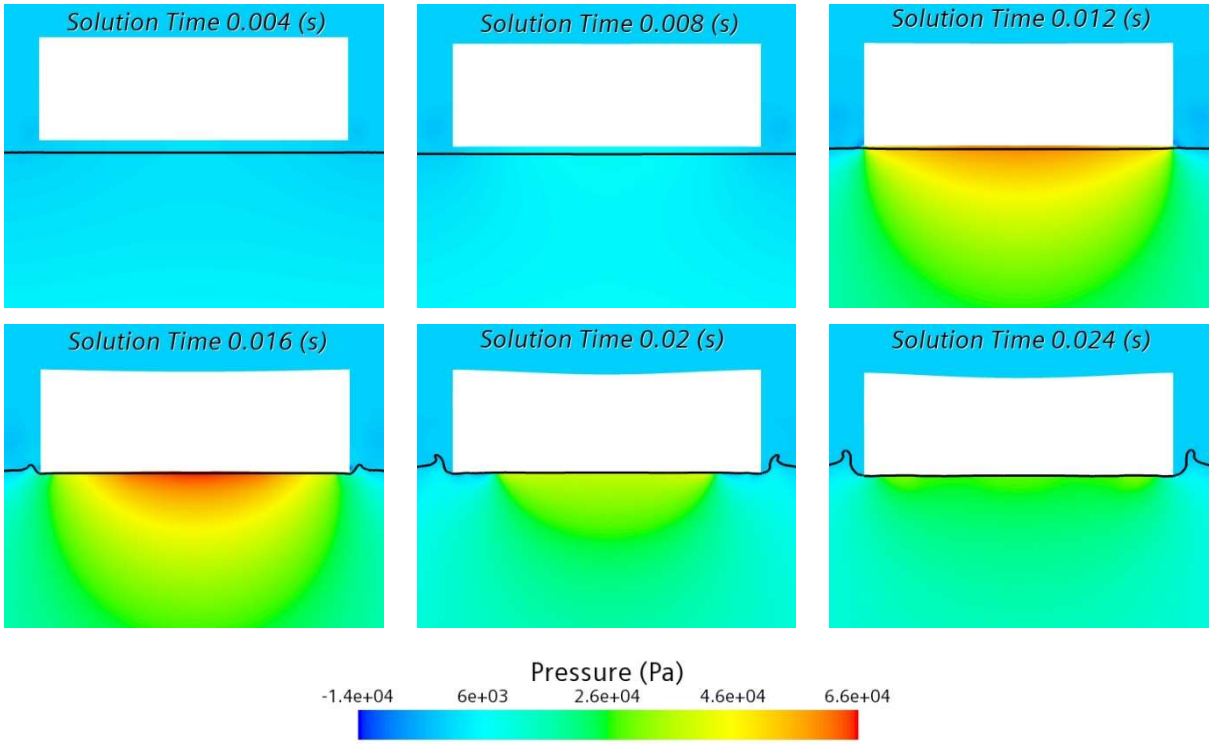

Fig. 20 Pressure distribution in the fluid domain during water entry

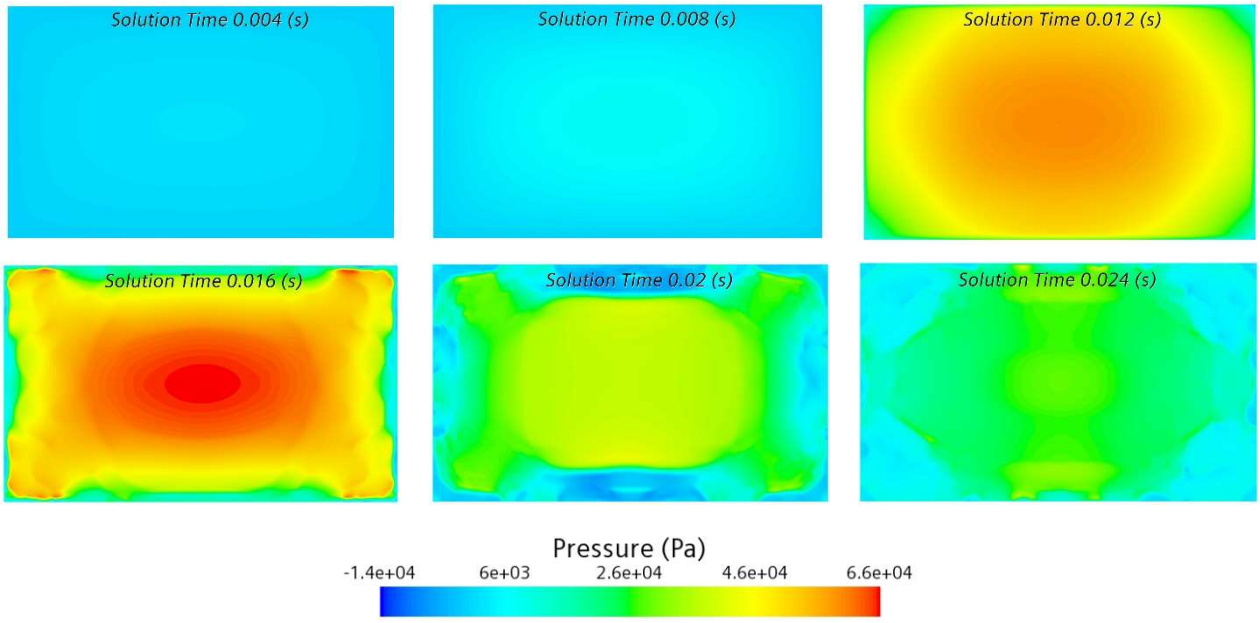

Fig. 21 Pressure distribution on the bottom surface during water entry

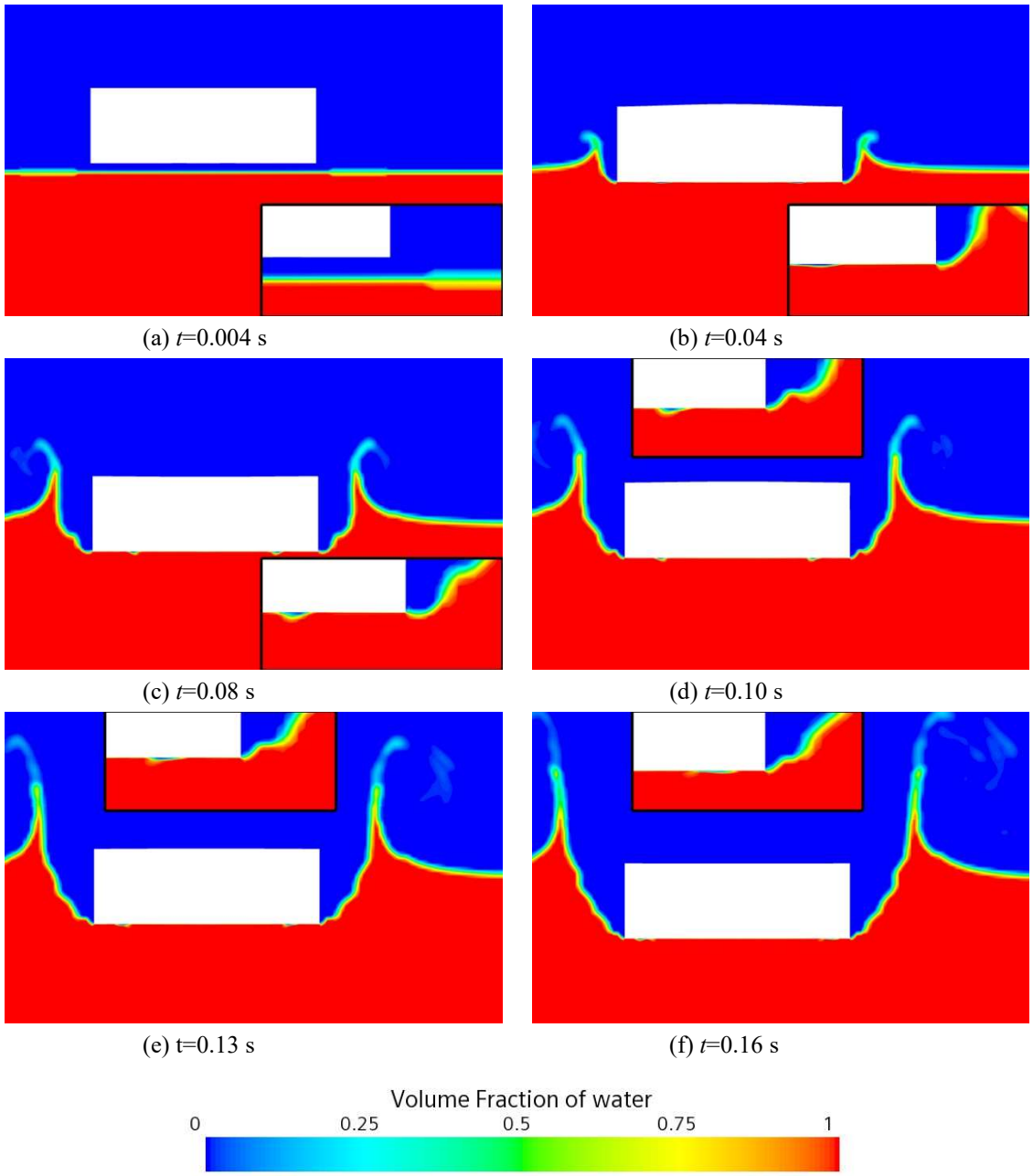

Fig. 22 Evolution of the volume fraction of water during water entry

Fig. 22 illustrates the temporal evolution of water volume fraction during the water entry process, where each subfigure includes a localized enlarged view of the bottom region. Initially, as the structure moves, the surrounding air enters the water. The deformation of the bottom plate contributes to the volume of air that is involved in the liquid, and the increasing deformation acts as a trigger for the formation of cavities within the liquid. It is worth noting that the distribution of the air layer is not uniform along the bottom, while it concentrates on areas where greater deformation occurs. As the bottom structure descends further, the encapsulated air escapes from the sides due to the deformation of the bottom plate. Eventually, a small amount of air remains trapped in the central region of the bottom plate.

5.2.2 Influence of structural damping

In the FE model, Rayleigh type damping is used:

$$\boldsymbol{C} = \alpha \boldsymbol{M} + \beta \boldsymbol{K} \tag{4}$$

where $\boldsymbol{C}$, $\boldsymbol{M}$ and $\boldsymbol{K}$ represent the structural damping matrix, structural mass matrix and structural stiffness matrix, respectively. The damping coefficients α and β are constant parameters that respectively correspond to mass proportional damping and stiffness proportional damping, and their values can be determined based on the specific material and structure. The mass proportional damping coefficient α predominantly influences low-frequency response, while the stiffness proportional damping coefficient β largely affects the high-frequency vibrations. In general, α and β can be evaluated by the following equations:

$$\alpha = \lambda_1 \omega_1 \tag{5}$$

$$\beta = \frac{\lambda_1}{\omega_1} \tag{6}$$

where λ_1 represents the damping ratio of the 1st order vibration and ω_1 is the natural frequency of the 1st order mode. These values were determined by referring to the experimental data, and β=0.0006 is used for all simulations in this paper. Fig. 23 compares the calculated pressure time series at P1 in Case 4 by different stiffness proportional damping coefficients of β=0.0003, 0.0006, 0.00095, and 0.0012. It can be observed that the high-frequency vibration component decreases with the increase in β; however, it has very small influence on the peak pressure value. Only the amplitude of high-frequency component is affected by the damping coefficient, while the frequency is not affected.

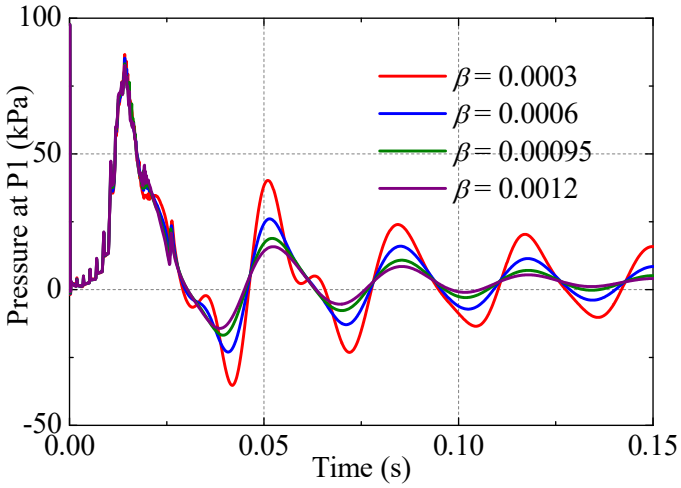

Fig. 23 Comparison of pressures at P1 under different structural damping ratios

5.2.3 Comparison between different methods

Xie et al. [23] conducted a study on the water entry problem of the same model using both uncoupled and coupled methods with the help of FLUENT and ANSYS software packages. Fig. 24 compares the pressure time series at P1 for Cases 2 and 4 by different methods including experiment and numerical simulations. It can be seen that the peak pressures vary among the methods, and the high-frequency components show some deviation in amplitude and phase. The results by the uncoupled method in Xie et al.'s work [23] and the present one-way coupled method do not contain any high-frequency component as the model is regarded as a rigid body, which means that the effect of structural elasticity is not considered in the simulation. Consequently, the model also tends to overestimate the pressure peak value, indicating that the elastic effect can mitigate the slamming pressure. For instance, in Case 4, the pressure peak at P1 obtained from the uncoupled method is approximately 31% higher than the experimental result. On the other hand, the peak values obtained by the two coupled methods (including the present study and that by Xie et al. [23]) exhibit good agreement with the experimental data for Case 4. However, for Case 2, the present method underestimates the peak pressure compared with the experiment, while the coupled method by Xie et al. [23] overestimates it. As previously discussed, the damping coefficient significantly affects the high-frequency components. Although there is a

phase difference, the high-frequency components demonstrate a similar trend for the experimental and the numerical results.

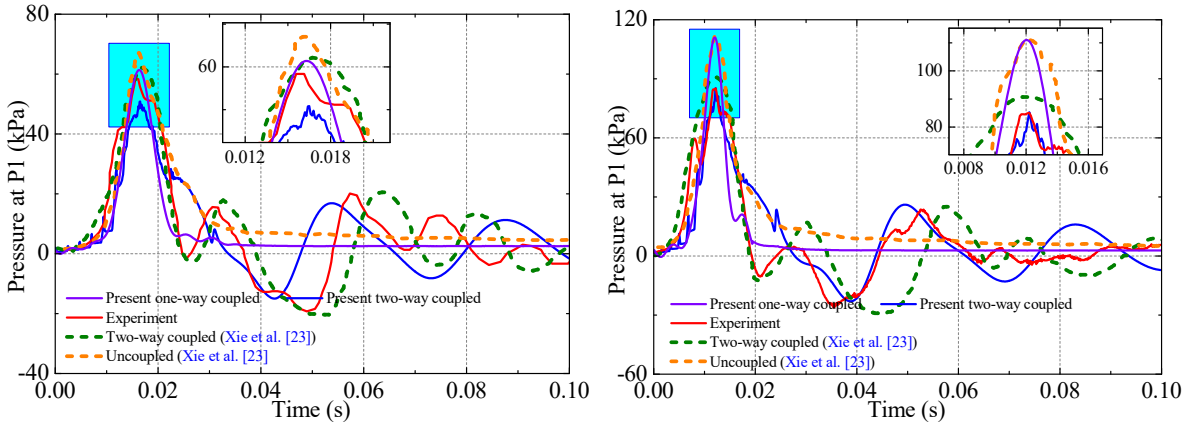

(a) Case 2 (b) Case 4

Fig. 24 Comparison of pressure time series at P1 for different methods

Table 7 presents a summary of the pressure peaks obtained at specific points (P1, P2, and P4) using various methods for Cases 2 and 4. The results indicate that in Case 2, the present method tends to underestimate the slamming pressure peak with a difference of less than 13%. Conversely, the coupled method used by Xie et al. [23] tends to overestimate it. However, it is worth noting that as the impact velocity increases, the present two-way coupled method demonstrates better accuracy. For example, the error in Case 4 is less than 2% when compared with the experiment.

Table 7 The pressure peak values obtained by different methods (in kPa)

Case	Position	Experiment	Uncoupled method (Xie et al. [23])		Two-way coupled method (Xie et al. [23])		Present one-way coupled		Present two-way coupled	
			Value	Error	Value	Error	Value	Error	Value	Error
2	P1	57.1	67.0	17.5%	62.2	9.0%	61.4	7.5%	50.8	–10.9%
	P2	59.6	71.4	19.8%	61.9	3.8%	62.1	4.2%	51.8	–13.0%
	P4	54.9	62.9	14.5%	58.7	7.0%	59.8	8.9%	48.3	–12.0%
4	P1	85.1	111.6	31.2%	90.7	6.6%	111.0	30.4%	85.3	0.2%
	P2	86.0	107.6	25.1%	89.5	4.0%	112.3	30.6%	86.5	0.6%
	P4	81.9	97.4	19.0%	92.3	12.7%	102.7	25.4%	81.0	–1.1%

5.2.4 Variation under different drop heights

Fig. 25 shows the numerical pressure results at P1 for different fall height cases with damping β=0.0006. Both the time series and the frequency spectra are presented for comparison. It can be seen that the pressure peak and fluctuation amplitude increase with the increase in drop height. The peak frequency (30 Hz) is almost the same for all cases, which is lower than the 1st order dry natural frequency (35.9 Hz) of the structure. As listed in Table 3, the first three orders of dry natural frequency of the model calculated by the Eigenvalue analysis of the FE model are 35.9 Hz, 50.7 Hz and 68.1 Hz, respectively. The 2nd and 3rd order vibrations are very weak and have little effect on the pressure results.

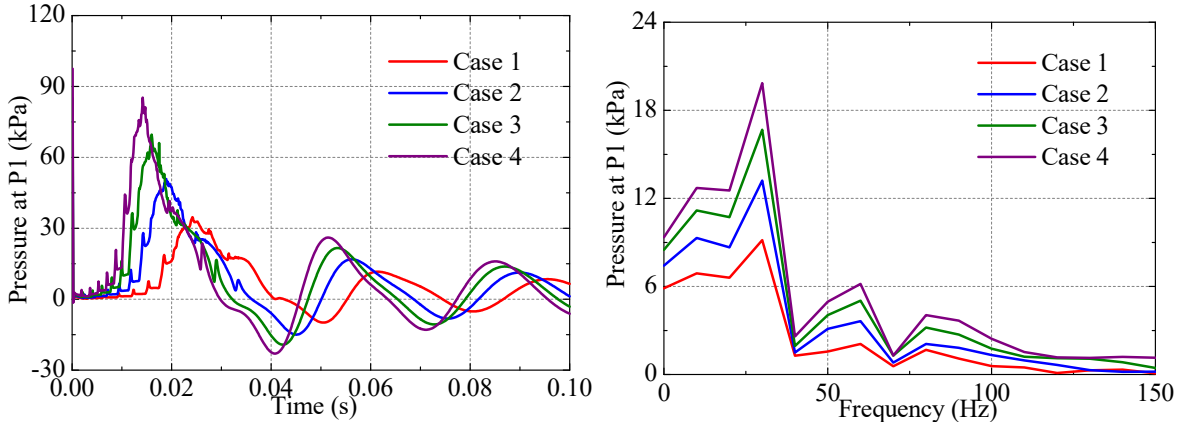

(a) Time series of pressure at P1 b) Frequency spectra of P1

Fig. 25 Pressure for different cases by numerical simulation

5.3 Structural stress and deformation

5.3.1 Stress distribution and symmetry

Fig. 26 illustrates the time series of axial stress at different positions of S1–6 for both the experimental and the numerical results. There is a certain difference in the trend of the two groups of curves: the stress peak of the numerical curves is sharper than that of the experimental ones. For these stress results, multiple phases can be observed due to structural flexibility, and the maximum stress occurs in the first phase. The bottom plate becomes wet and begins to oscillate during the initial stage. Then, the stress decreases in the subsequent stage or phases. However, this phenomenon is different from the result described by Faltinsen [6]. Therein, the plate became wet at the end of phase one, then vibrated in the following phases and the maximum stress occurred at phase two. The stress peaks are distributed in an order of S5>S2>S4>S1 for both the experimental and the numerical results. Theoretically, when a flat panel with its four sides rigidly fixed is subjected to a uniform surface pressure load, the largest stress distributes at the center and the stress decreases from the center to the four edges. This shows similar behaviour with the stress distribution on the bottom plate of this paper.

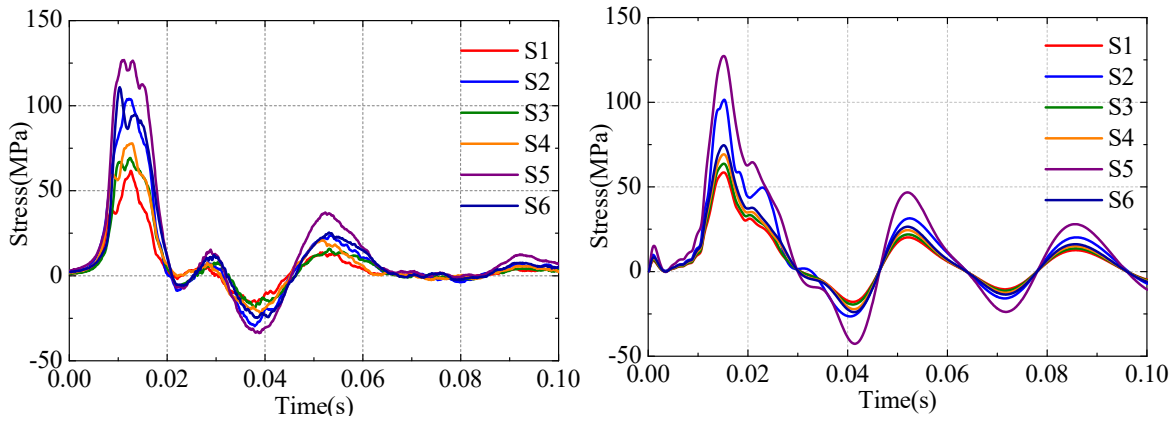

(a) Experimental data (b) Numerical data

Fig. 26 Comparison of stress at different positions (Case 4)

The corresponding frequency spectra by FFT of the time series results of Case 4 for both experiment and numerical simulation are compared in Fig. 27. There are two dominant peaks in the experimental spectra, that is, around 25 Hz and 50 Hz. Similarly, there are also two dominant peaks in the numerical spectra located at approximately 31.2 Hz and 56.2 Hz. Compared with the experimental spectra, the numerical spectra have higher 1st order spectral peak values and lower 2nd order spectral peak values.

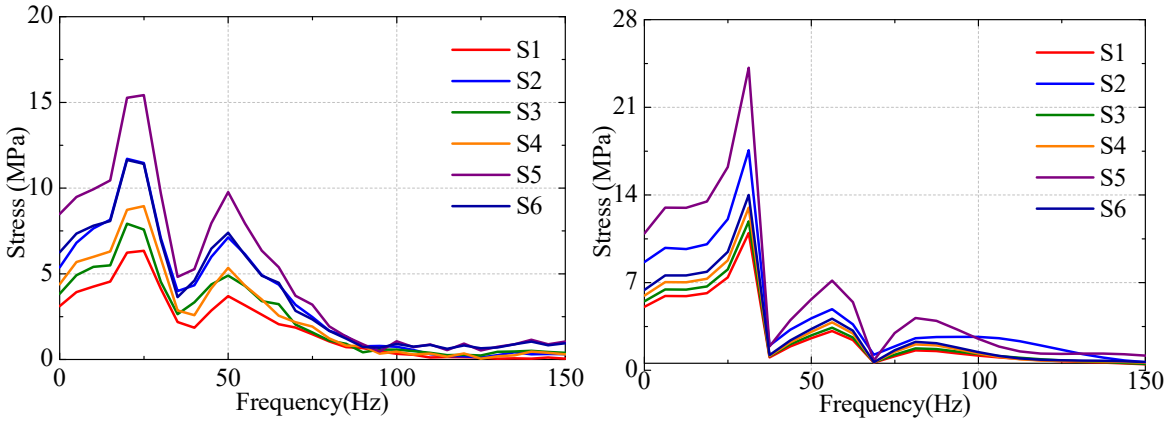

(a) Experimental data (b) Numerical data

Fig. 27 Comparison of stress spectra (Case 4)

5.3.2 Influence of structural damping

Next, the influence of stiffness proportional damping coefficient β on the stress is studied. The calculated stress time series at S5 in Case 4 by different stiffness proportional damping coefficient β=0.0003, 0.0006, 0.00095 and 0.0012 are compared in Fig. 28. To have similarity with the pressure data, the high-frequency vibration component decreases with the increase in β, along with the slight decrease in the peak value, which is more pronounced than the pressure data.

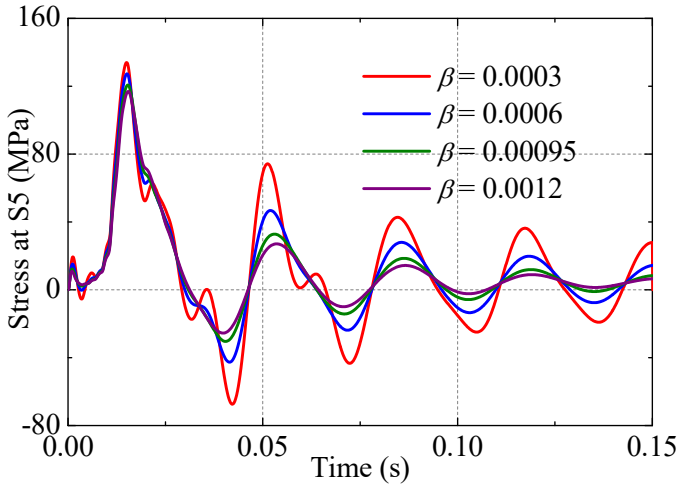

Fig. 28 Comparison of stress at S5 under different structural damping ratios

5.3.3 Comparison between methods

Fig. 29 shows the comparison of axial stress at S5 between the four different methods for Cases 2 and 4. In the figure, the present method results are for the damping β=0.0006. At the initial impact stage (t<0.025 s), both coupled numerical solutions (the current paper and that of Xie et al. [23]) agree well with the experimental results regarding the peak value and phase shape of curve. However, the uncoupled solution and the present one-way coupled method both overestimate the stress peak value. In Case 4, the stress peak at S1 by the uncoupled solution in [23] is about 42% larger than the experimental result, while the difference is only below 6% for the present two-way coupled solution. Additionally, there are high-frequency oscillations in the experimental result, whereas neither the uncoupled solution nor the one-way coupled method shows such oscillations. The two-way coupled methods provide reasonable prediction for the high-frequency responses in amplitude (the error is less than 10% compared with the experimental data), but the phase is different. In general, the uncoupled solution cannot reproduce the high-frequency vibrations due to the rigid body assumption. On the other hand, the numerical method considers the air cavity but not the compressibility of

fluid, which could result in error as the fluid compressibility may be nonnegligible under the condition of high impacting pressure.

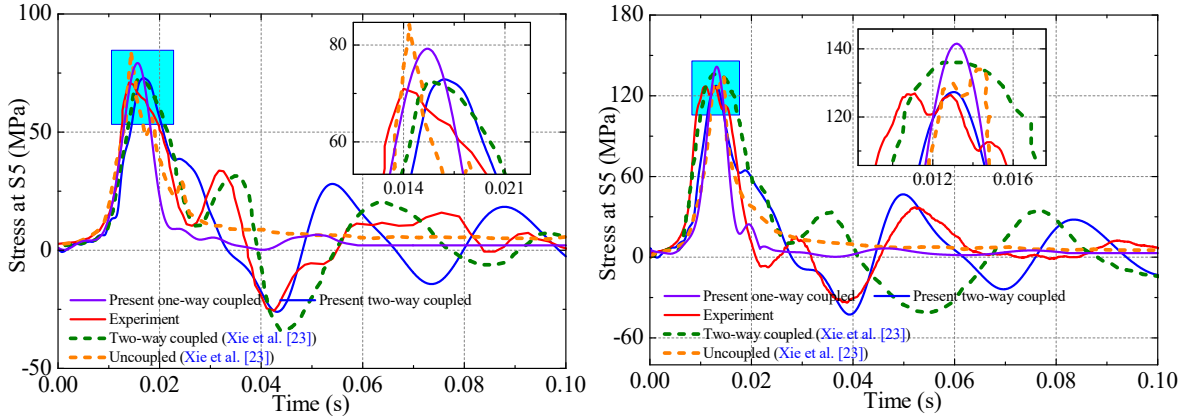

(a) Case 2 (b) Case 4

Fig. 29 Comparison of stress at S5 between different methods

Table 8 summarizes the stress peaks at typical points S1, S2 and S4 for different methods for Cases 2 and 4. The stress on the bottom longitudinal bone differs significantly at different positions. The uncoupled method largely overestimates the stress with a maximum difference of 42%. The two-way coupled method in the research of Xie et al. [23] slightly overestimates the stress peak with a difference below 5.7%. Meanwhile, the present two-way coupled method underestimates the stress peak with a difference below 12%.

Table 8 Comparison of stress peak value between different methods (in MPa)

Case	Position	Experiment	Uncoupled method (Xie et al. [23])		Two-way coupled method (Xie et al. [23])		Present one-way coupled		Present two-way coupled	
			Value	Error	Value	Error	Value	Error	Value	Error
2	S1	34.2	41.0	19.9%	36.2	5.7%	33.6	–1.8%	30.3	–11.5%
	S2	59.1	61.4	3.8%	61.9	4.6%	67.9	14.9%	57.9	–2.1%
	S5	72.5	85.9	18.4%	74.7	3.0%	79.2	9.2%	72.9	0.5%
4	S1	61.7	87.6	41.9%	62.7	1.5%	62.9	1.9%	58.5	–5.2%
	S2	104.0	126.6	21.7%	109.5	5.2%	124.6	19.8%	101.5	–2.5%
	S5	126.9	136.4	7.5%	132.3	4.2%	141.5	11.5%	127.3	0.3%

5.3.4 Variation with different drop heights

Fig. 30 shows the numerical stress results at S5 for different fall height cases. Both the time series and the frequency spectra are presented for comparison. It is seen that the stress peak and fluctuation amplitude increase with the rise in drop height. The peak frequency (30 Hz) is almost the same for all the cases and is a little lower than the 1st order dry natural frequency (35.9 Hz).

Table 9 summarizes the axial stress peak value for the results of different undamped cases. It is seen that the stress peaks distribute in an order of S5>S2>S6>S4>S3>S1 for the numerical results. In addition, the difference between the symmetric measuring points S1 and S3 is below 9%, whereas it is 8% for S4 and S6. In Case 4, the largest axial stress 127.32 MPa occurs at S5, which is much lower than the yield stress of high-strength aluminium. Therefore, the hydroelasto-plasticity problem is not taken into account in the present numerical simulation. In fact, this can be considered by defining the parameter of plasticity in the material property module of Abaqus.

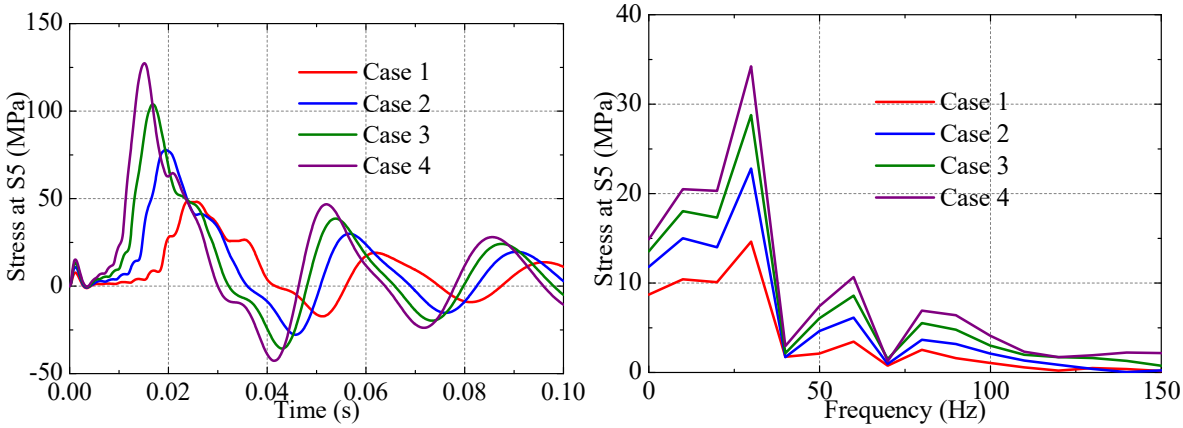

(a) Time series of pressure at S5 b) Frequency spectra of S5

Fig. 30 Stress in different cases by numerical simulation

Table 9 Statistics of the peak value of axial stress in different cases

Case	S1	S2	S3	S4	S5	S6
1	20.57	39.56	22.61	24.38	48.36	25.94
2	30.30	57.90	33.30	36.45	72.93	39.60
3	43.36	82.29	47.74	51.98	103.83	56.50
4	58.53	101.46	63.68	69.22	127.32	74.57

Fig 31. shows the von Mises stress distribution on the bottom structure at the time instant (t=0.015 s) when the stress peak occurs and the corresponding structural deformation is enlarged by 30 times. Due to the upwards fluid loads on the bottom plate, a hogging bending phenomenon occurs on the longitudinal bones. The highest stress is observed at the connection between the longitudinal bone and the bottom plate. The largest von Mises stress is about 100 MPa, and the most obvious structural deformation occurs at the middle cross-section of the middle longitudinal bone.

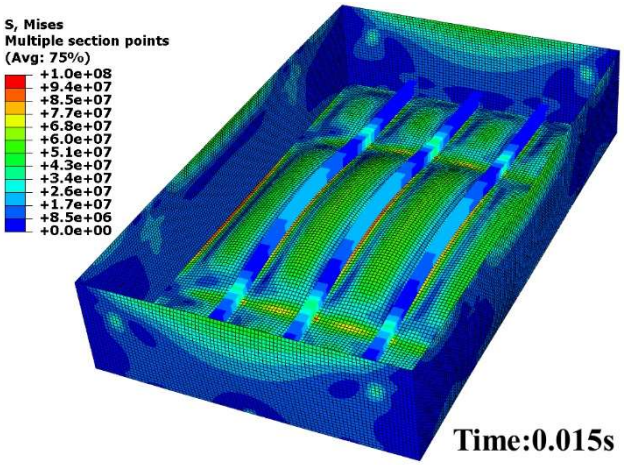

Fig. 31 Stress distribution on the bottom plate at peak stress (Case 4, unit: Pa)

During the water entry process, the structure experiences vibrations at its natural frequency. Fig. 32(a) illustrates the maximum and minimum stress phases during the first high-frequency vibration period, which occur at 0.0408 s and 0.0511 s, respectively. The figure also displays the distribution of normal stress and structural deformation (enlarged by 30 times) on the bottom structure at these two phases. Additionally, Fig. 32(b) includes a comparison of the corresponding stress distribution on the deck plate (enlarged by 10 times) at the same time instants as in Fig. 32(a). Due to the contribution of stiffeners, the deformation of the bottom plate is significantly less pronounced than that of the deck plate.

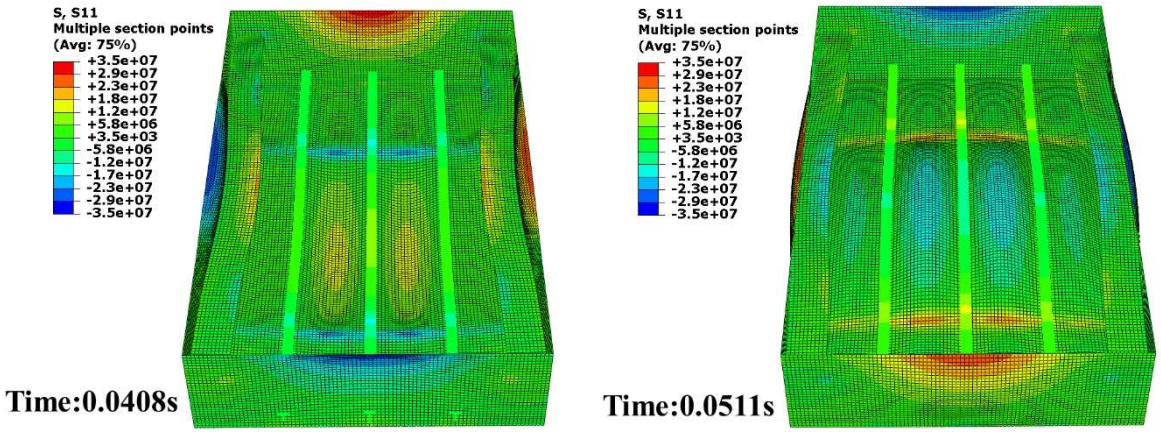

(a) Bottom structure

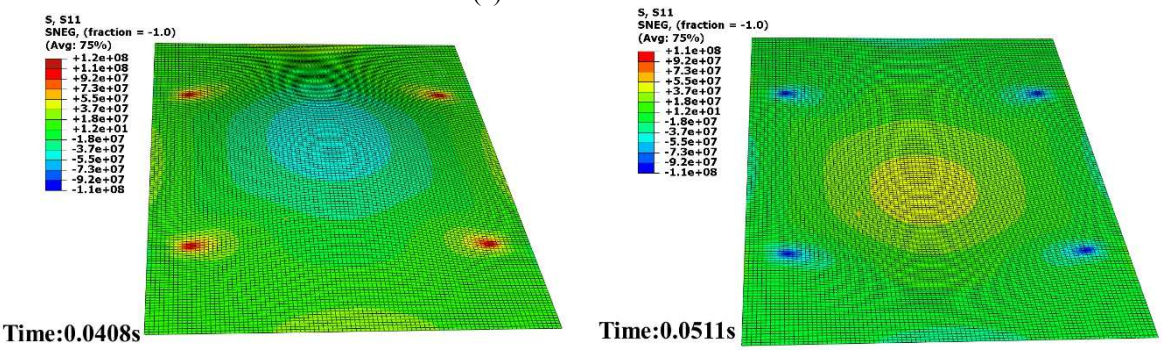

(b) Deck plate

Fig. 32 Stress distribution and structural deformation at typical vibration phases (Case 4, unit: Pa)

5.4 Influence of inner stiffeners on slamming behaviour

In order to investigate the effect of inner stiffeners on slamming loads and hydroelastic response, two additional models, that is, without or with partial stiffeners, are established and used for simulations. A comparison of the three models and their FE grid models are presented in Fig. 33. Ballast mass is mounted on the two new models so that the weight of the three models is identical.

Additional simulations regarding the model without or with partial stiffeners under the condition of Case 4 are performed. Fig. 34 compares the results of vertical motions and loads responses between the results by the three models with different inner stiffener arrangements. As seen from Fig. 34(a) and (b), the three curves for vertical displacement and velocity are almost the same at the beginning stage during the free fall motion in air. Then, the model without stiffeners moves ahead of the remaining two models as it has a smaller speed loss. However, after 0.06 s, the model without stiffeners falls behind, probably due to the large deformation and vibration of its bottom plate, which can be seen from the comparison of water volume fraction variation presented in Fig. 35.

Fig. 34(c) and (d) compare the time series of impact pressure at P1 and the structural stress at S5 between the three models with different inner stiffener arrangements. The original model has the largest pressure peak, while the model without stiffeners exhibits the smallest pressure peak. The pressure reduction of the model without stiffeners can be attributed to the air cavitation effect. However, the aftereffect for the three models is quite different due to different vibration mode behaviour. The hydroelastic vibration after the first impact peak of the two models with or without partial stiffeners is more obvious and they have a greater vibration period than the original model. On the other hand, the stress of the two models with or without partial stiffeners is much greater than that of the original model due to the lack of reinforcing stiffeners.

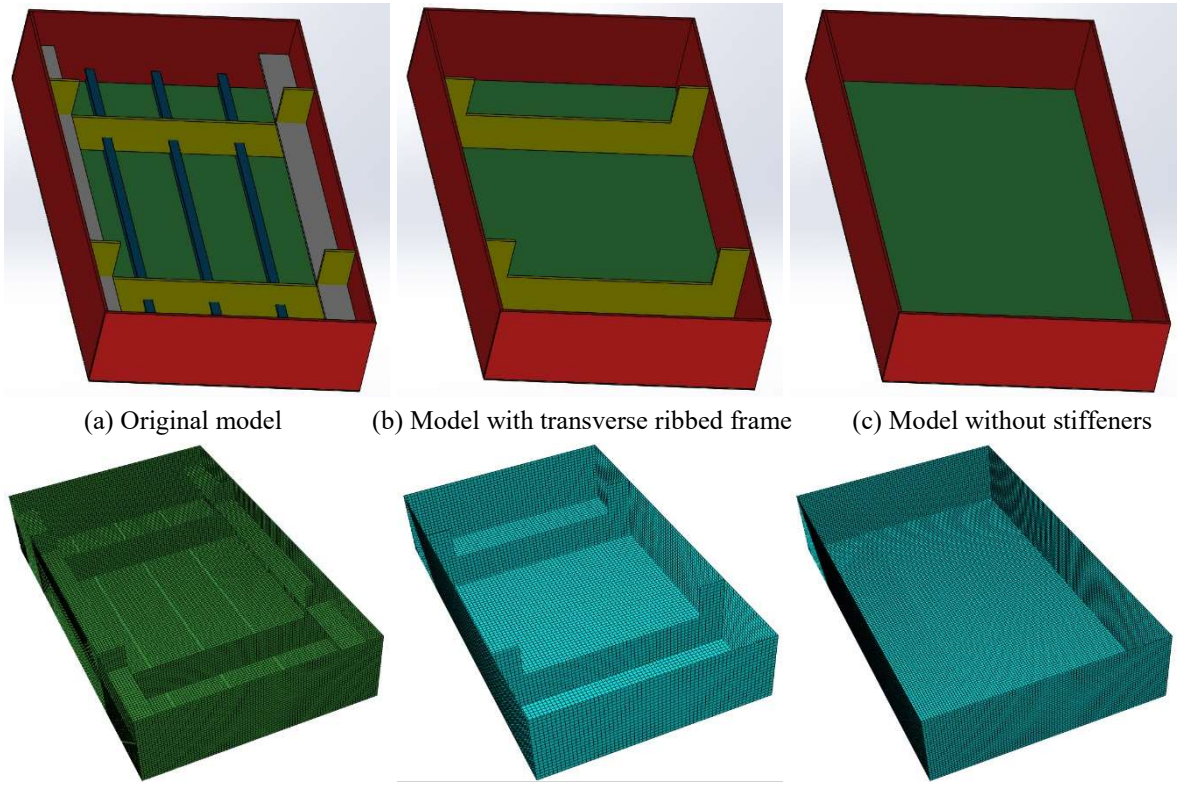

(a) Original model (b) Model with transverse ribbed frame (c) Model without stiffeners

(d) FE model of the original model (e) FE model with transverse ribbed frame (f) FE model without stiffeners

Fig. 33 Geometric and FE model of the hull structure with different arrangements of the inner stiffeners

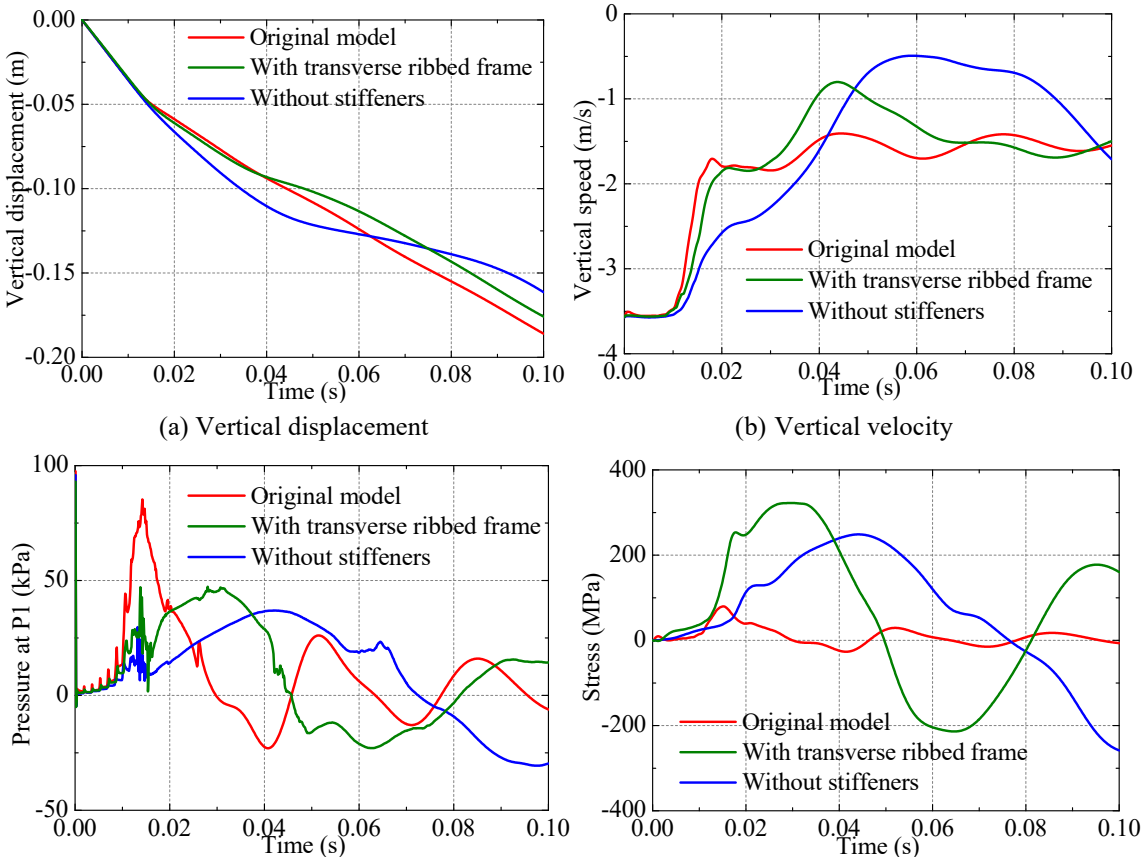

(a) Vertical displacement (b) Vertical velocity

(c) Impact pressure at P1 (d) Structural stress at S5

Fig. 34 Comparison of vertical motions and load responses between the three models

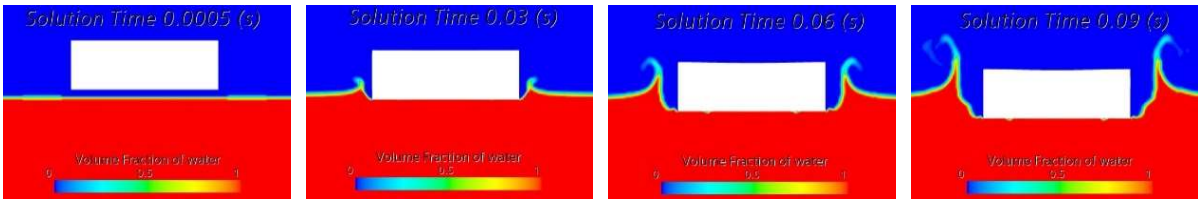

(a) Original model

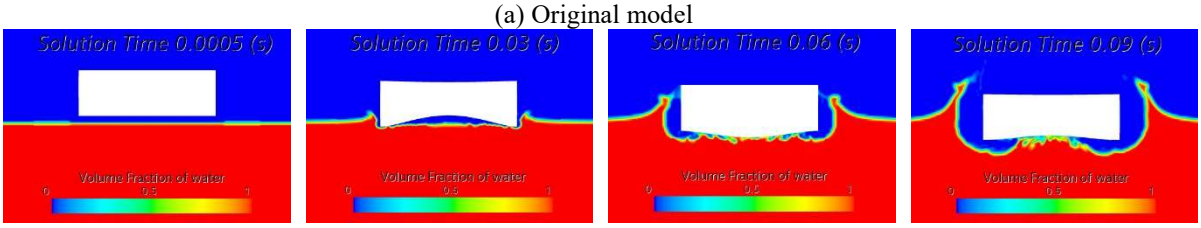

(b) Model with transverse ribbed frame

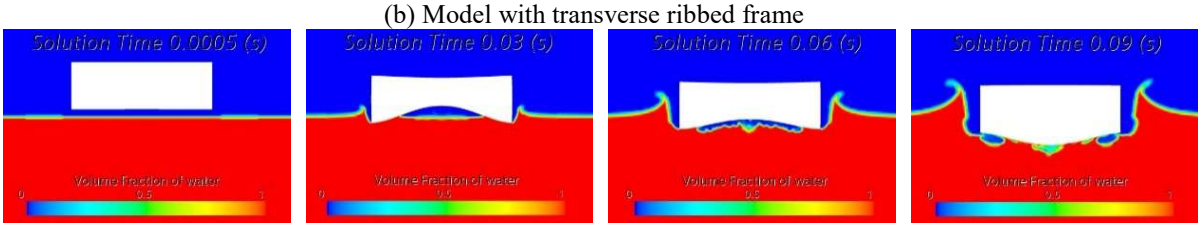

(c) Model without stiffeners

Fig. 35 Evolution of volume fraction of water during water entry: a comparison between the three models

6. Conclusions

This paper presents a CFD-FEM two-way coupled method for the simulation of water entry process of a flexible aluminium flat stiffened plate structure. The slamming load behaviour and structural response of the structure in different water entry conditions are investigated and compared with the results of other methods. The following conclusions can be drawn:

(1) The structural flexibility effect on slamming behaviour is non-negligible. The present CFD-FEM method well simulates almost all fluid-structure interaction characteristics such as displacement, speed, acceleration, slamming loads, structural stresses, and deformation, as well as produces graphical visualizations of interest within the scope of the slamming issue.

(2) The stiffness proportional damping coefficient β largely affects the high frequency mode. In the fluid pressure and structural stress results, the high-frequency vibration component decreases with the increase in β. It also has slight influence on decreasing the peak value especially for stress.

(3) The peak pressures or stresses by different methods are close, but the high-frequency components show obvious deviation in amplitude and phase. The results of uncoupled or one-way coupled method do not contain any high-frequency components. The peak values in the two two-way coupled methods (including the present paper and Xie et al. [23]) show good agreement with the experimental data but the phase may be different.

(4) Compared with the model without stiffeners or with partial stiffeners, the model with stiffeners produces the largest pressure peak but the lowest stress. Structural flexibility and deformation can reduce the impact pressure. The hydroelastic vibration after the first impact peak of the model without stiffeners is more obvious and has a greater vibration period than the model with stiffeners.

The present CFD-FEM coupled method can be employed to solve a wide range of hydro-dynamic, wave load and hydroelasticity problems of ships and offshore structures. For example, it can be used to simulate the seakeeping problem of ships operating in waves. The motions, global loads, local loads, and structural stress can be obtained for ship design and the optimization of body plan and structure details. In future work, the numerical method can be further developed and improved based on some open source codes such as OpenFOAM and CalculiX instead of commercial software.

Acknowledgments

This research is supported by the National Natural Science Foundation of China (No. 52271316) and the Guangdong Basic and Applied Basic Research Foundation (No. 2023A1515030262).

REFERENCES

[1] Kapsenberg, G. K., 2011. Slamming of ships: where are we now? *Philosophical Transactions of the Royal Society A*, 369, 2892–2919. https://doi.org/10.1098/rsta.2011.0118

[2] Wang, X., Yang, P., Gu, X., Hu, J., 2015. Review of the theoretical investigation of slamming of global wave loads on ship structures. *Chinese Journal of Ship Research*, 10(1), 7-18.

[3] von Karman, T., 1929. The impact on seaplane floats during landing. *NACA Technical Note*, No. 321.

[4] Wagner, H., 1932. Uber stoss-und gleitvorgange an der oberflache von flussigkeiten. *Zeitschrift für Angewandte Mathematik und Mechanik*, 12(4), 193-235. https://doi.org/10.1002/zamm.19320120402

[5] Xu, G., Duan, W., 2009. Review of prediction techniques on hydrodynamic impact of ships. *Journal of Marine Science and Application*, 8(3), 204-210. https://doi.org/10.1007/s11804-009-8039-7

[6] Faltinsen, O. M., 2000. Hydroelastic slamming. *Journal of Marine Science and Technology*, 5(2), 49–65. https://doi.org/10.1007/s007730070011

[7] Yu, P., Li, H., Ong, M., 2019. Hydroelastic analysis on water entry of a constant-velocity wedge with stiffened panels. *Marine Structures*, 63, 215–238. https://doi.org/10.1016/j.marstruc.2018.09.007

[8] Han, B., Peng, Y., Li, H., Liu, S., Sun, S., Shan, Y., Sun, Z., 2022. Numerical investigations of a 2D bow wedge asymmetric free-falling into still water. *Ocean Engineering*, 266, 112905. https://doi.org/10.1016/j.oceaneng.2022.112905

[9] Das, K., Batra Romesh, C., 2011. Local water slamming impact on sandwich composite hulls. *Journal of Fluids and Structures*, 27(4), 523-551. https://doi.org/10.1016/j.jfluidstructs.2011.02.001

[10] Sun, S. Y., Sun, S. L., Wu, G., 2015. Oblique water entry of a wedge into waves with gravity effect. *Journal of Fluids and Structures*, 52, 49–64. https://doi.org/10.1016/j.jfluidstructs.2014.09.011

[11] Zhang, G., Feng, S., Zhang, Z., Chen, Y., Sun, Z., Zong, Z., 2021. Investigation of hydroelasticity in water entry of flexible wedges with flow detachment. *Ocean Engineering*, 222, 108580. https://doi.org/10.1016/j.oceaneng.2021.108580

[12] Sun, S., Liu, B., Zhang, A., 2019. On the fully nonlinear water entry of a cone in Stokes wave. *Engineering Analysis with Boundary Elements*, 98, 232–242. https://doi.org/10.1016/j.enganabound.2018.10.019

[13] Tang, H, Wan, Q, Ren, H., 2023. Numerical study of trimaran wave load based on time-domain Rankine method. *Brodogradnja*, 74(3), 107-129. https://doi.org/10.21278/brod74306

[14] Chuang, S., 1970. Investigation of impact of rigid and elastic bodies with water. *Report for Department of the Navy*. Washington, DC, United States Department of the Navy, Report No.: 3248.

[15] Ma, Z., Causon, D., Qian, L., Mingham, C., Mai, T., Greaves, D., Raby, A., 2016. Pure and aerated water entry of a flat plate. *Physics of Fluids*, 28, 016104. https://doi.org/10.1063/1.4940043

[16] Yan, D., Mikkola, T., Kujala, P., Hirdaris, S., 2023. Hydroelastic analysis of slamming induced impact on stiff and flexible structures by two-way CFD-FEA coupling. *Ships and Offshore Structures*, 18(9), 1300-1312. https://doi.org/10.1080/17445302.2022.2116231

[17] Stenius, I., Rosén, A., Battley, M., Allen, T., 2013. Experimental hydroelastic characterization of slamming loaded marine panels. *Ocean Engineering*, 74, 1-15. https://doi.org/10.1016/j.oceaneng.2013.09.007

[18] Yan, D., Mikkola, T., Lakshmynarayanana, A., Todter, S., Schellin, T. E., Neugebauer, J., el Moctar, O., Hirdaris, S., 2022. A study into the FSI modelling of flat plate water entry and related uncertainties. *Marine Structures*, 86, 103296. https://doi.org/10.1016/j.marstruc.2022.103296

[19] Wang, S., Islam, H., Guedes Soares, C., 2021. Uncertainty due to discretization on the ALE algorithm for predicting water slamming loads. *Marine Structures*, 80, 103086. https://doi.org/10.1016/j.marstruc.2021.103086

[20] Fang, X., Ming, F., Wang, P., Meng, Z., Zhang, A., 2022. Application of multiphase Riemann-SPH in analysis of air-cushion effect and slamming load in water entry. *Ocean Engineering*, 248, 110789. https://doi.org/10.1016/j.oceaneng.2022.110789

[21] Sun, H, Wang, D., 2018. Experimental and numerical analysis of hydrodynamic impact on stiffened side of three-dimensional elastic stiffened plates. *Advances in Mechanical Engineering*, 10(4), 1687814018767705. https://doi.org/10.1177/1687814018767705

[22] Wang, D., Wu, L., Zhu, Y., Wang, X., Li, Y., 2019. Vibration of a plate coupled with fluid considering the effects of stress and deformation under hydrostatic load. *Thin-Walled Structures*, 145, 106413. https://doi.org/10.1016/j.tws.2019.106413

[23] Xie, H., Ren, H., Qu, S., Tang, H., 2018. Numerical and experimental study on hydroelasticity in water-entry problem of a composite ship-hull structure. *Composite Structures*, 201, 942-957. https://doi.org/10.1016/j.compstruct.2018.06.030

[24] Cheon, J., Jang, B., Yim, K., Lee, H., Koo, B., Ju, H., 2016. A study on slamming pressure on a flat stiffened plate considering fluid–structure interaction. *Journal of Marine Science and Technology*, 21, 309–324. https://doi.org/10.1007/s00773-015-0353-y

[25] Truong, D., Jang, B., Janson, C., Ringsberg, J., Yamada, Y., Takamoto, K., Kawamura, Y., Ju, H., 2021. Benchmark study on slamming response of flat-stiffened plates considering fluid-structure interaction. *Marine Structures*, 79, 103040. https://doi.org/10.1016/j.marstruc.2021.103040

[26] Truong, D., Jang, B., Ju, H., Han, S., 2021. Prediction of slamming pressure considering fluid-structure interaction. Part II: Derivation of empirical formulations. *Marine Structures*, 75, 102700. https://doi.org/10.1016/j.marstruc.2019.102700

[27] Truong, D., Jang, B., Ju, H., Han, S., 2022. Prediction of slamming pressure considering fluid-structure interaction. Part I: numerical simulations. *Ships and Offshore Structures*, 17, 7-28. https://doi.org/10.1080/17445302.2020.1816732

[28] Xie, H., Ren, H., Li, H., Tao, K., 2019. Quantitative analysis of hydroelastic characters for one segment of hull structure entering into water. *Ocean Engineering*, 173, 469-490. https://doi.org/10.1016/j.oceaneng.2019.01.011

[29] Jiang, Y., Sun, Z., Zong, Z., Sun, Y., Jin, G., 2021. Effects of air cushion on slamming load of trimaran cross-deck structure. *Chinese Journal of Ship Research*, 16(5), 197–205.

[30] Lakshmynarayanana, P., Temarel, P., 2019. Application of CFD and FEA coupling to predict dynamic behaviour of a flexible barge in regular head waves. *Marine Structures*, 65, 308-325. https://doi.org/10.1016/j.marstruc.2019.02.006

[31] Lakshmynarayanana, P., Temarel, P., 2020. Application of a two-way partitioned method for predicting the wave-induced loads of a flexible containership. *Applied Ocean Research*, 96, 102052. https://doi.org/10.1016/j.apor.2020.102052

[32] Paik, K., Carrica, P., Lee, D., Maki, K., 2009. Strongly coupled fluid–structure interaction method for structural loads on surface ships. *Ocean Engineering*, 36(17), 1346-1357. https://doi.org/10.1016/j.oceaneng.2009.08.018

[33] Piro, D., Maki, K., 2013. Hydroelastic analysis of bodies that enter and exit water. *Journal of Fluids and Structures*, 37, 134-150. https://doi.org/10.1016/j.jfluidstructs.2012.09.006

[34] Chen, Z., Jiao, J., Wang, Q., Wang, S., 2022. CFD-FEM simulation of slamming loads on wedge structure with stiffeners considering hydroelasticity effects. *Journal of Marine Science and Engineering*, 10(11), 1591. https://doi.org/10.3390/jmse10111591

[35] Takamia, T., Matsuia, S., Oka, M., Iijima, K., 2018. A numerical simulation method for predicting global and local hydroelastic response of a ship based on CFD and FEA coupling. *Marine structure*, 59, 368-386. https://doi.org/10.1016/j.marstruc.2018.02.009

[36] Monroy, C., Seng, S., Benhamou, A., Malenica, S., de Lauzon, J., 2018. A methodology for hydro-structure simulations based on OpenFOAM®. *8th International Conference on HYDROELASTICITY IN MARINE TECHNOLOGY (HYEL)*, Sep. 10-12, Seoul, Korea.

[37] McVicara, J., Lavroff, J., Davis, M.R., Thomas, G., 2018. Fluid-structure interaction simulation of slam-induced bending in large high-speed wave-piercing catamarans, *Journal of Fluids and Structures*, 82, 35-58. https://doi.org/10.1016/j.jfluidstructs.2018.06.009

[38] Shi, Y., Pan, G., Yim Solomon, C., Yan, G., Zhang, D., 2019. Numerical investigation of hydroelastic water-entry impact dynamics of AUVs. *Journal of Fluids and Structures*, 91, 102760. https://doi.org/10.1016/j.jfluidstructs.2019.102760

[39] Sun, T., Zhou, L., Yin, Z., Zong, Z., 2020. Cavitation bubble dynamics and structural loads of high-speed water entry of a cylinder using fluid-structure interaction method. *Applied Ocean Research*, 101, 102285. https://doi.org/10.1016/j.apor.2020.102285

[40] Iijima, K., Kimura, K., Xu, W., Fujikubo, M., 2011. Hydroelasto-plasticity approach to predicting the post-ultimate strength behavior of a ship's hull girder in waves. *Journal of Marine Science and Technology*, 16, 379-389. https://doi.org/10.1007/s00773-011-0142-1

[41] Liu, W., Luo, W., Yang, M., Xia, T., Huang, Y., Wang, S., Leng, J., Li, Y., 2022. Development of a fully coupled numerical hydroelasto-plastic approach for offshore structure. *Ocean Engineering*, 258, 111713. https://doi.org/10.1016/j.oceaneng.2022.111713

[42] Chen, Z., Jiao, J., Wang, S., Guedes Soares, C., 2023. CFD-FEM simulation of water entry of a wedged grillage structure into Stokes waves. *Ocean Engineering*, 275, 114159. https://doi.org/10.1016/j.oceaneng.2023.114159

[43] Lakshmynarayanana, P.A.K., Hirdaris, S., 2020. Comparison of nonlinear one- and two-way FFSI methods for the prediction of the symmetric response of a containership in waves. *Ocean Engineering*, 203, 107179. https://doi.org/10.1016/j.oceaneng.2020.107179

[44] Wilson, R., Carrica, P., Stern, F., 2006. Unsteady RANS method for ship motions with application to roll for a surface combatant. *Computers & Fluids*, 35(5), 501–524. https://doi.org/10.1016/j.compfluid.2004.12.005

[45] Saydam, A. Z., Küçüksu, G. N., İnsel, M., Gökçay, S., 2022. Uncertainty quantification of self-propulsion analyses with RANS-CFD and comparison with full-scale ship trials. *Brodogradnja*, 73(4), 107-129. https://doi.org/10.21278/brod73406

[46] Mikulec, M., Piehl, H., 2023. Verification and validation of CFD simulations with full-scale ship speed/power trial data. *Brodogradnja*, 74(1), 41-62. https://doi.org/10.21278/brod74103